MASTER'S DEGREE IN BIOMEDICAL ENGINEERING

Influence of Tissue Mechanics in Blood Vessel Growth

Author:

António Luís Correia

Centre for Computational Physics

Faculty of Science and Technology

University of Coimbra

Supervisor:

Rui D.M. Travasso

Centre for Computational Physics

Faculty of Science and Technology

University of Coimbra

Dissertation presented to the University of Coimbra in fulfilment of the requirements necessary for obtaining a MSc degree in Biomedical Engineering.

July, 2012

Abstract

Sprouting angiogenesis, the process of creating new blood vessels from pre-existing vasculature, is a fundamental routine in the animal body, being responsible for growth and development, wound healing and, in some cases, pathologies.

Conditions such as cancer and diabetic retinopathy can be treated with the aid of drugs or strategies developed using new knowledge of how blood vessel growth occurs. Some of the results of pre-existing knowledge are already applicable in healthcare, such as antiangiogenic drugs.

Over the last 30 years, researchers have come up with some mathematical models to simulate vascular growth, focusing in specific aspects or a simplified overview of the process. However, almost none of the proposed models account for the mechanical environment experienced by the cells of the capillary network.

This work's goal is to rectify this gap by incorporating mechanical features in a continuum model of angiogenesis. This model is a phase-field approach to the problem that bridges the macroscopic and microscopic descriptions of the process.

The successive steps that were taken from beginning with a standard phase-field model, deriving and integrating the mechanical equations and experimenting with several control parameters are documented and discussed in each appropriate section.

For each step, several possibilities on how to control the system in a way that remained closely tied to the biology perspective were considered. Emulating the tension that the tip cells exert on the extracellular medium by incorporating its analytical description in the equations was chosen.

The results gave enough information that corroborated the success of incorporating mechanical tension in the model, as the vessels that were simulated responded in the way it was expected.

In some cases regression of vessels was observed. This is an important result as, despite being very present in the Biological literature, it had not been successfully modelled within this type of approach.

Sumário

O processo de criação de novos vasos sanguíneos a partir de vasculatura pré-existente, uma das formas do fenómeno chamado de angiogénese, é fundamental no corpo humano, sendo importante em crescimento e desenvolvimento, cicatrização de feridas e, nalguns casos, em processos patológicos.

Tanto patologias do foro oncológico como outras, como a retinopatia diabética, podem ser tratadas com ajuda de fármacos ou estratégias desenvolvidas com base no conhecimento do desenvolvimento e formação de novos vasos sanguíneos. Este tipo de conhecimento tem aplicações já relativamente comuns, como em terapia com fármacos anti-angiogénicos.

Ao longo dos últimos 30 anos, equipas de investigação desenvolveram modelos matemáticos que simulam crescimento vascular, tanto através de aspetos específicos deste processo como através de uma visão mais global e simplificada do mesmo. No entanto, nestes modelos não estão incluídas as caraterísticas mecânicas do meio celular, que influenciam grandemente as células da rede capilar.

O objetivo deste trabalho passa por preencher esta lacuna, incorporando caraterísticas mecânicas num modelo contínuo do processo angiogénico. Este modelo será uma aproximação *phase-field* ao problema, de forma a abranger e juntar as caraterísticas macroscópicas da população e microscópicas de alguns elementos-chave.

Os passos sucessivos que foram tomados, desde o início, simulando um modelo *phase-field* canónico, derivação e integração das equações mecânicas e experimentação e teste de vários parâmetros de controlo, estão neste trabalho documentados e discutidos (nas secções apropriadas).

Em cada passo várias possibilidades de formas de controlar o sistema de forma a que este se mantivesse fiel à Biologia do caso real foram consideradas. Emular a força que as células da ponta exercem no meio extra-celular incorporando a sua descrição analítica nas equações foi a forma que escolhemos.

Nalguns casos observámos regressão dos vasos recém-formados. Este resultado, descrito na literatura referente à biologia, não tinha sido ainda corretamente modelado dentro deste tipo de abordagem.

Acknowledgements

I want to thank Professor Rui Travasso for giving me the opportunity to learn about subjects which had been a growing interest of mine during the Biomedical Engineering course. I was able to gain experience in problem solving and modelling and work on a supercomputer cluster, which was a fabulous experience. He was also responsible for allowing me to attend reunions and meetings, which enlightened me about some of the responsibilities of a researcher. His enduring patience and uplifting personality were great motivators in this work.

I must thank Professor Miguel Oliveira for allowing me to attend his classes on Parallel Computing. He took time to explain every doubt or problem I came upon, although I was not enrolled in the class.

I thank the group at *Centro de Física Computacional* for letting me attend their reunions as it was instructive and demonstrative of a real working environment.

I would also like to thank my girlfriend, Ana Sílvia for her continued support at every step, for her dedication in helping me by proof-reading and media editing and for her overall patience.

I must also acknowledge that this work is financed by FEDER Funds through the Programa Operacional Fatores de Competitividade – COMPETE and by National Funds through FCT – Fundação Para a Ciência e a Tecnologia in the scope of project FCOMP-01-0124-FEDER-015708.

Contents

List of Figures

List of Tables

Introduction

1.1 Motivation

Angiogenesis is the vital process of creating and restructuring blood vessels. Evidently, it is of great importance in various physiological routines, such as wound healing, embryonic growth and inflammation[25,29,33]. However, it is also pivotal in several pathological situations (over 70*), such as rheumatoid arthritis, diabetic retinopathy (i.e. retinal damage caused by diabetes) and tumour growth. In the latter case, extensive studies have been undertaken, in part because of the high mortality rates. Although there is much research on tumour angiogenesis, new information is surfacing every day and the community has not reached a consensus on its main mechanics[3].

Medically, angiogenesis knowledge is used in adjuvant therapy. This can branch in two opposite concepts: angiogenic stimulative therapy and antiangiogenic therapy, which inhibits angiogenesis.

Tumours can be starved of their blood supply by using antiangiogenic therapies. Without blood supply, a tumour would never grow enough in size to be significantly harmful and malignant, as the necessary growth stimulant nutrients and oxygen are cut off. Moreover, increased vascularization of tumours raises the probability of the tumour metastasising[30]. In this case, antiangiogenic procedures could stop cancerous tumours from proliferating and metastasising, thus decreasing their risk of being fatal[8]. Additionally, these treatments can normalise the tumour's vasculature to permit better delivery of chemotherapeutic drugs and oxygen, which will increase the efficiency of radiation therapy.

Therapeutic angiogenesis, in contrast, stimulates angiogenesis where it is required but lacking. This technique is used to replenish the blood supply to chronic wounds in order to speed healing, and it helps prevent unnecessary amputations. In addition, this approach can be also used to save limbs afflicted with poor circulation, and even oxygen-starved hearts. Other conditions that are caused by insufficient angiogenic stimulus are ischaemic heart disease and preeclampsia. Angiogenesis stimulation therapies may even help to regenerate damaged or lost tissues such as nerves and brain tissue.

To better understand the factors that influence blood vessel growth, approaches from the fields of Mathematics and Physics play an important role. Currently, the input from these fields is key on the research on angiogenesis and it can serve as a stepping stone to develop better approaches to the broader problems that are influenced by vascular dynamics. Researchers of these fields commonly use the aid of computer modelling and simulation to tackle the biological principles underlying these issues. By modelling the basic principles inherent to the system studied, they can reach conclusions about more

*according to the Angiogenesis Foundation: 'http://www.angio.org/'

complex issues that depend or can be connected to them. Hence, by using computer simulations, the core mechanics of the problem studied can be tested and understood.

The existent research has achieved models that simulate certain steps[33] or even the entire angiogenic process[31]. Yet, a scarce amount of models account for the mechanical effects of the neighbouring tissues on blood vessel growth and their effect during angiogenesis. Furthermore, these effects are non-negligible on one of the most crucial steps during angiogenesis – sprout migration and proliferation. Thus, by including the interplay between the inherent mechanical characteristics of the system and its evolution, a more accurate emulation of angiogenesis can be created.

Consequently, better simulations lead to improved predictive capability as well as provide information that increases our understanding of angiogenesis, blood vessel growth and restructuring. With this data, a better contribution can be made to research on the broader problems of tumour growth and tissue regeneration.

1.2 Objectives

The development of a phase-field model that included the mechanical effects was the main goal of this work. Our model is included in the continuum model type and uses a force field to incorporate and manipulate migration in accordance to the known mechanics. However, the quantitative parametrisation of the model was not one of the goals of this work.

The first step taken in this work was to better acquaint myself with these types of models, by simulating already existing models and understand their properties and equations.

Then, we proceeded with deriving equations that described the elastic characteristics of the system and compare them with the literature available. In our case, the approach used to modelling these mechanical effects was only applied before in the context of Materials Science[23], hence, this kind of implementation to study a biologic process is pioneering. Thus, to test the viability of working with a phase-field in this topic we extensively simulated various outcomes that increased our awareness of its potential and its underlying principles.

With this data, we devised ways to manipulate and control the system so that it would mimic blood vessel growth.

These several stages followed the typical progress in experimental modelling; each stage supplied information about the general viability or viable direction to take in the subsequent stage. Specifically, in this work we tried to verify if the several manipulations we induced on the system were in accordance with the biological information available.

These stages and the full model statement will be given in the Model Development chapter. Only the last step in the model, which includes the know-how of all the previous steps, will be discussed through its results on the appropriately named Exploring the Model chapter.

An additional objective proposed was parallelizing the code to work in a shared memory system, such as the computational cluster present at the *Departamento de Física*. This entailed attending classes on Parallel Computing that taught the fundamentals of code parallelization through openMP and MPI in two different computer languages, C/C++ and Fortran.

The final goal was documenting the work done and discussing it in the form of a thesis that would later be reviewed.

In conclusion, through these tasks, several techniques from Mathematics and Physics were used to deepen the knowledge of a topic with Biological and Medical relevance. This resulted in an interdisciplinary work that bridged the areas mentioned, which we believe is the goal of the Biomedical Engineering course to which this work was proposed.

1.3 Molecular Biology Background

This work entails a complex biologic process that has several components around it that are important for the global understanding and appreciation of the angiogenic routine.

Features of these components will be used throughout the work. To clarify some of choices that were made when deriving the mathematical model, specifically those made to accommodate the biologic content, a short introduction of the different mechanisms and components of relevance to angiogenesis follows below.

1.3.1 Endothelial Cells

Endothelial cells constitute the endothelium, a thin layer that lines the interior of blood and lymphatic vessels. This layer forms an interface between the vessel wall and the lumen, where blood flows.

The endothelium is a specialised epithelial tissue. The distinction between endothelial and other epithelial cells comes from their origin during embryogenesis.

Being a lining to blood and lymphatic vessels, the endothelium has the ability to form different kinds of junctions with its surrounding tissue. These adhesion and communication complexes' types and features depend on a great amount of factors, like the type of vessel and the characteristics of the structure it perfuses.

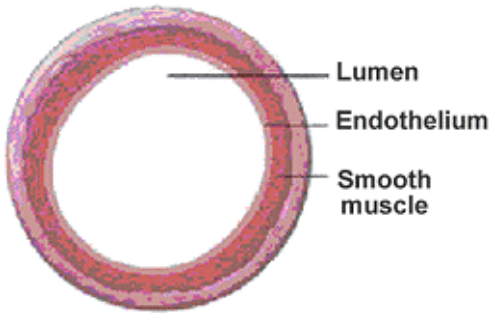

Figure 1.1: Blood vessel cross-section image indicating the position of the lumen and endothelial cells.

There are mainly three types of cell junctions: gap junctions, which are communication structures that allow the passage of small molecular solutes between neighbouring cells; tight junctions, that act mainly as a barrier, regulating permeability and maintaining cell polarity, and adherens junctions, that play an important part in contact inhibition of endothelial cell growth. In addition, these junctions are of extreme importance for a correct organization of new vessels in angiogenesis.

The adherens junctions form a continuous adhesion belt, called *zonula adherens*, that encircles the interacting cells in the tissue[2]. By connecting directly to the actin cytoskeleton of the cell, this junction allows for resilient and slightly elastic behaviour. Hence, they are relevant in cell migration.

The endothelium acts as a semi-selective barrier, controlling the passage of materials and the transit of white blood cells into or out of the bloodstream. Endothelial cells are able of internalizing large molecules present in the extracelular medium, thus enabling transport of molecules between the lumen of the vessel

and the rest of the vessel wall[19].

If in direct contact with blood, these cells are called vascular endothelial cells. These line the entire circulatory system, from the heart to the smallest capillaries, and have specific functions, including fluid filtration (e. g. in the kidney), blood vessel tone (i.e. vasoconstriction and vasodilation), hemostasis and hormone signalling.

1.3.2 Pericytes

Pericytes are cells commonly present in the endothelial layers of capillary blood vessels in the brain. They are important in the maintenance of the blood-brain barrier and other homeostatic functions. In this topic, pericytes are important because of their functions as blood flow regulators and monitors of endothelial cell maturation and dormancy. Also, they are one of the main type of cells that produce collagen, the most abundant protein in vertebrates, which is used mainly for structural support (e.g. as a component of the Extracellular Matrix).

They are associated with permitting endothelial cells to differentiate, multiply, migrate, and form vascular branches. In addition, they have somewhat inelastic and stiff properties, granting some measure of rigidity and stability to the blood vessels' wall.

New views grant the pericytes further capabilities of blood vessel remodelling and influence on endothelial cell migration[10], increasing their significance in the context of this work.

1.3.3 Actin

Actins are proteins found in most eukaryotic cells, especially in their cytoskeleton. They normally assemble themselves into long, linear polymers, called microfilaments. Microfilaments are involved in changing cell shape and maintaining its structure, due to their flexible, but resilient properties. In addition, when aggregated with myosin (a motor protein), forming a bulkier polymer, actomyosin, they are able to contract and elongate. These characteristics are fundamental for cell movement.

Actin polymerization is, naturally, directional, having a growing end. In the opposing edge, actin monomers are recovered through disassembly. Thus, recycling of actin monomer occurs continuously, freeing monomers necessary to fuel the expanding end.

1.3.4 Extracellular Matrix

Normally abbreviated to ECM, the extracellular matrix is the non-cell part of a tissue and it is one of the most abundant complexes in the animal body. As such, it is an important component in supplying structural support in the body. Moreover, it is also important in controlling the cell's dynamic behaviour, as it can sequester growth factors in its mesh[15]. These can be released by degrading part of the ECM's matrix by using specific protein degrading enzymes called proteases. This type of activity occurs naturally during cell migration, mediated by the cells themselves. It is important to note that by accumulating growth factors, some types of rapid growth are possible without synthesizing the growth factors from scratch.

The extracellular matrix can be divided into two main branches: the basement membrane and the interstitial matrix. The space between cells is occupied by the interstitial matrix, which is filled with fibrous proteins and long polysaccharides. This enables it to support the various stresses forced upon it by other cells and tissues[1]. The other constituent, the basement membrane, acts as a surface scaffold on which epithelial cells rest. Effectively, it anchors the epithelium to the lower substrates, increasing its protective role as a mechanical barrier against pathogens and malignant cells. Recently, it was concluded that the basement membrane also plays an important role in angiogenesis by accelerating endothelial cell differentiation[14].

1.3.5 Integrins

An integrin is a receptor protein that mediates and makes possible the attachment between a cell and the surrounding tissues. Yet, integrins do not function solely as mechanical links to the neighbouring tissues; they also give important information about the nature of the cell's surroundings. They dynamically cooperate with signals from receptors in the cellular membrane and enforce cellular decision on what action to take (e.g. movement, differentiation). Integrins are present on the surface of most cells in the human body.

Nevertheless, in the context of this work, the integrin's main role is the adhesion between endothelial cells and the extracellular matrix. Here, integrins function as hooks, grabbing a strand of the extracellular matrix. Mediated by other molecules, they can connect to the cell's actin cytoskeleton. Integrin's connections to the ECM can take the form of large, stable adhesions (i.e. focal adhesions)[32] or small, transient adhesions (i.e. nascent adhesions) that can mature into larger adhesions or disassemble[9]. As such, they function as mechanical anchorage between movement starting actins and the reasonably static extracellular matrix.

1.3.6 Cell Migration

Cell movement during angiogenesis is a very important concept. This biologic context will clarify the need to include the mechanical properties of the system into a coherent model of the angiogenic process. Cell migration can be divided into four distinct steps.

Polarization

In migrating cells, polarization is the propensity of forming structurally different fronts and rears, with distinct roles. This polarity arises from directional cues influencing the migration present in the system. These directional cues can be chemotactic (caused by varying concentrations of chemoattractants in a soluble fluid), haptotactic (where the gradient of chemoattractants is bound on a surface), mechanotactic (fluidic shear stress), or some combination of these.

The cell's leading edge usually has a protrusion generated by a high degree of actin polymerization. Also on the forward end, adhesion to the vicinity is accomplished by means of integrins. On the opposite edge, disassembly and release (i.e. recycling) of both microfilament monomers and adhesive integrins occurs.

Protrusion

A protrusion is the extension of the membrane in the direction of migration (i.e. the leading edge). These protrusions are dubbed pseudopodia. Depending on their appearance, several classifications exist; in endothelial cell movement, the most common type of pseudopodia is filopodia, which are thin, slightly fusiform, and mostly filled by ectoplasm.

To form a filopodium, three steps need to happen sequentially:

1. Expansion of the plasma membrane;

2. Formation of an underlying backbone that supports membrane extension;

3. Establishment of contacts with the surrounding layers to provide traction.

The traction created by integrin links facilitates the movement of the rest of the cell body. The protrusion is produced by local actin polymerization. Filopodia are comprised of actin microfilaments that are arranged into long parallel bundles. Due to their 'spike-like' arrangement, filopodia are able to probe the medium in the direction they are projected and are especially well attuned to find mechanotactic cues.

Adhesion

Adhesion to the surrounding medium is mediated by integrin receptors. By forming links to the surrounding layers, integrins also trigger signalling pathways that regulate (i.e. promote or inhibit) the formation of protrusions. As mentioned, they connect the extracellular medium to the actin cytoskeleton, thus providing traction for migration.

Adhesion can only occur at specific sites on the cell's surface. These vary in shape and size, from the big, circular focal adhesions to the small and elliptic nascent adhesions. Their shape and size also carry physiological implications: the smaller types are able to promote faster actin polymerization and recycling and, therefore, are better suited for fast migration[7]. Also, the adhesion site's size is a relevant factor pertaining to its strength; smaller sites usually provide less robust links than bigger adhesion spots.

Cell Movement

Cell translocation by contraction of actomyosin is not well understood[21]. However, forward movement is possible due to actomyosin contraction. As the actin cytoskeleton is linked to the ECM by integrins on adhesion points, actin polymer contraction at the adhesion site will exert a compressive force. This force would pull the actin cytoskeleton forward, along with the cell body, and the ECM back towards the force's focus. As this force is equal in both directions, the net movement should be zero. However, due to the polarity of actin polymerization (assembly at the front and disassembly at the back) and the relative strength of the adhesion contacts, there is a bias towards forward cell movement[16,21]. Furthermore, because of the static traits of the extracellular matrix, pulling on this substrate leaves it relatively unmoved while having a significant increase in movement for the cell.

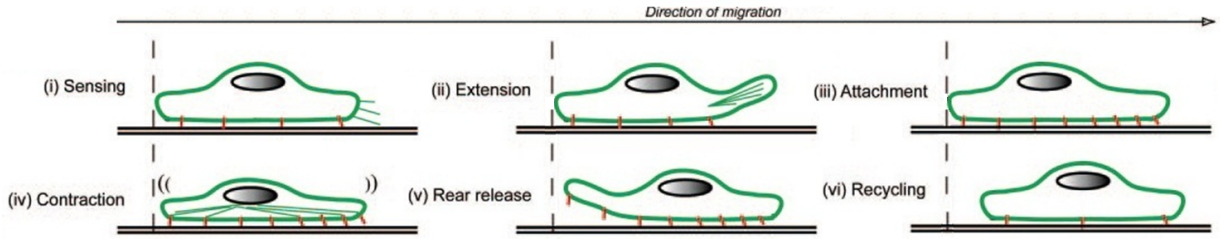

Figure 1.2: Simplified scheme of cell movement with descriptive stage names that illustrates the integrin-actin dynamics.

The rear end's retraction is the result of the disassembly of the adhesion spots at the lagging end[22] and recycling of actin polymers. These factors combined with proteolytic cleavage of the proteins linking integrins to microfilaments, create a detached rear end that will move itself towards the cell body's middle[16].

1.4 Angiogenesis

Angiogenesis is the physiological process of blood vessel growth from pre-existing vasculature. It is specially relevant in development and growth[29]. This phenomenon is present in embryogenesis, where it creates rich microvasculatures with minimal energy dissipation[5].

Withal, it is also pivotal for wound healing. A wound creates a low-oxygen environment locally (i.e. hypoxia), which will cause cells to release angiogenic stimulating factors. Due to the hypoxia, cells only have anaerobic metabolism available, which outputs lactic acid. Both the hypoxia state and the consequent presence of lactic acid stimulate endothelial proliferation towards the wound. Thus, angiogenesis restructures the existent vasculature to create blood vessels in order to supply the wound with adequate blood flow. When the oxygen and nutrient needs of the area surrounding the wound have been met, angiogenic factors stop being released, as the cells are no longer exposed to an abnormal environment. In turn, this will signal reduced proliferation and subsequent apoptosis of unnecessary blood vessels[11].

However, angiogenesis is also a determinant factor in several pathological cases. The most predominant and more extensively studied is the influence of blood vessel growth in tumour development. Tumour growth, because of its high metabolic rate caused by its rapid cell division, relies heavily on blood irrigation for nourishment. Without sufficient blood flow the tumour's cells would enter a state of hypoxia. Although the surface cells may have sufficient irrigation, the core cells have a very restricted amount of oxygen and nutrients. It follows that at the the tumours' core, because of the hypoxia, there is production of lactic acid. While this dynamic is maintained, the core cells eventually enter apoptosis, as nutrients and oxygen become scarcer over time. The confined nature of the inner cells due to the fast growth migration restrictions causes a necrotic area at the tumour's centre[30]. In this stage, a tumour is classified as non-threatening. Notwithstanding, it is in this stage that is begins actively searching for nourishment. The contribution of the state of hypoxia and the presence of lactic acid stimulate the production of angiogenic factors. These will stimulate neighbouring vessels to proliferate towards the tumour and supply it with the materials it needs to proliferate and grow in size.

The cases mentioned above are enough to understand some of the roles that angiogenesis takes in some important physiologic processes, both natural and pathological.

Depending on the progression, role, or place where angiogenesis occurs, it can be classified as one of two types: intussusceptive angiogenesis and sprouting angiogenesis.

1.4.1 Intussusceptive Angiogenesis

This type of angiogenesis, also called splitting angiogenesis, forms new vessels by splitting existing ones. The capillary vessel wall protrudes into the lumen and continuously extends itself until it connects with the opposite wall, creating a split capillary vessel. It consists of four main phases.

In the first phase, direct contact of opposite located cells is established by protrusion of the vessel's walls into the lumen until contact is made. Usually, the contact spot is a very dense area, populated by inter-endothelial adherence zones in the opposite wall, while the initial movement spot is very contractible. This initiation process is normally attributed to the contractile motion of the vessel wall,

however, recently, hydrodynamic forces have been invoked as a potential agent[30].

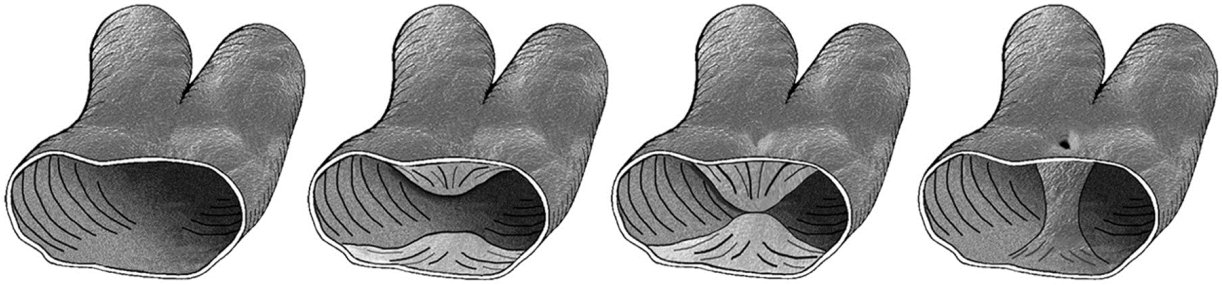

Figure 1.3: Sequence of steps that lead to the formation of a septum.

After having made contact, the cell's walls form a cylindrical bridge extending across the lumen. This is accomplished by reorganizing cell junctions and allowing both the vessel's bilayer and the basal membrane to be perforated. This tissue bridge is very thin and only enveloped by endothelial cells. Precursor cells to the extracellular matrix, along with pericytes, gradually fill the inside of the cylinder's core.

Then, the core's cells begin layering collagen, important fibres for the growth of the extracellular matrix. The interstitial space is still not able to support the usual dynamics present on blood vessels. However, the collagen matrix layered will soon have the myriad of components necessary to become an actual ECM, which will support the growth of the vessel's lumen.

After the last step, the blood vessel will be locally divided into two smaller vessels; two vessels separated by a mature septum. By merging these septa continuously it is possible to effectively 'split' the entire vessel along its length as seen of figure 1.4.

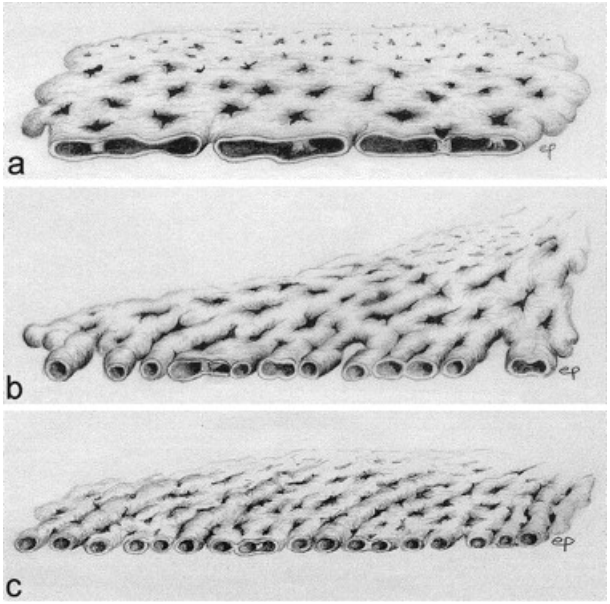

Figure 1.4: Septa continually merging to form vast capillary networks from a small amount of vessels.

A noticeable advantage of this type of angiogenesis is that it can occur without increasing significantly

the number of endothelial cells by instead reorganizing the existing cells into a greater number of capillary vessels. Because of this, it is a very common process during embryonic growth and development, where cell creation is more costly (i.e. cell division has a very high energy expenditure). In addition, because it does not rely on cell proliferation, which in ample scale is slow, these restructuring phenomena can occur in a matter of hours or even minutes[5].

1.4.2 Sprouting Angiogenesis

In the sprouting counterpart, new cells are created when forming the new blood vessel. It usually follows well-defined stages. First, signalling proteins are released by tissue cells, possibly following rupture or lack of oxygen concentration. These proteins are commonly growth factors; in this study, we emphasise the Vascular Endothelial Growth Factor (VEGF). This factor and its influence on angiogenesis is the most commonly studied[13,18].

Upon its release, this signal causes a response in endothelial cells of close-by vessels. Blood vessels are usually in a dormant state, entrapped in pericytes. In this state, they are spatially constricted and are not capable of migrating. The response elicited by the growth factors changes the endothelial cells to their activated state. When this happens, several cascading effects start occurring; one of the most significant is the release of enzymes called proteases. These enzymes degrade the vessel's wall proteins, which are its main constituent, allowing endothelial cell's migration. In the following step, a part of the endothelial network begins its migration, using its tip region to sense directional cues. By following these cues, it is able to migrate in the direction of the source of the released factors.

Soon, the migrating cells start to resemble a sprout, with sensory tips and long stalks. The sprout's tips have the role of probing the environment for concentrations of growth factors. However, because there is only one tip cell for each stalk, it has a limited scope of perception of the flow and concentration of soluble factors. This role specialization allows for different areas to be probed simultaneously. Moreover, cells can have different amounts of growth factor receptors, which represent different sensibility. Thus, it is possible for some cells to migrate in wrong directions if they incorrectly sense the direction of the growth stimulus. Actually, recent studies[13] show that for this very reason, there is competition for tip cell position between cells with different receptor amount distribution and concentration. Understandably, this competition arises from natural selective pressure, forcing the population as a whole (i.e. instead of controlling each cell individually) to migrate in the correct direction.

The stalks are pushed along by the migration, because these strands of cells are interconnected tightly by adherens junctions. Furthermore, the cells proliferate quickly during migration to compensate for the massive difference in cell density created by the migration itself. At this stage, proliferation can be triggered by the soluble growth factors or even the mechanical stimulus of the force exerted for traction[16]. Nevertheless, the increase of proliferation fuels the endothelial stalk with new material, contributing greatly to the migration's success.

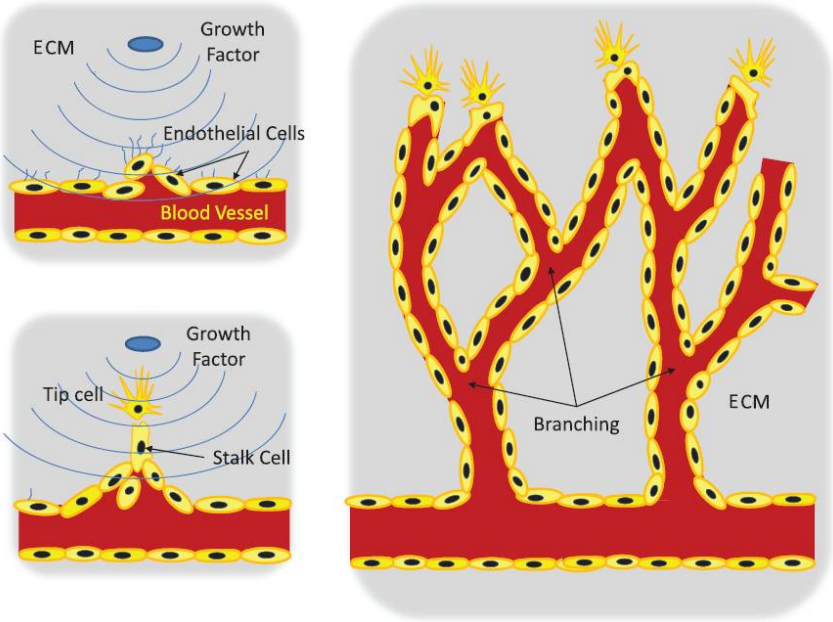

Figure 1.5: Simplified illustration of the some important steps and components of sprouting angiogenesis.

When the sprout connects to the target source of factors, usually a vessel, it forms loops creating a lumen. Then, it begins maturing, promoting the proliferation and migration of pericytes. Their influence will return the endothelial cells to its dormant state, as their concentration reaches the necessary level, creating a vessel capable of sustaining blood flow.

When blood flow is established on the proto-vessel, the final steps of maturation occur, which are related to several signal cascades that are outside of the scope of this work, resulting in a full-fledged blood vessel.

From these steps, we can conclude that sprouting angiogenesis has invasive characteristics and is, thus, able to bridge vascular gaps, which is evidenced in its presence during wound healing. However, it is a slow process because it relies heavily on cell proliferation and, in most cases, soluble cues, which diffuse slowly[5].

1.5 Mathematical Models Overview

Currently, several approaches to modelling angiogenesis (or parts of it) have been implemented. As any biological process, blood vessel growth depends upon other routines that are equally complex, having several different signalling molecules and receptors, distinct signal transduction cascades and dynamics. Thus, any model starts with a simplification of this intricate conglomerate of processes, both in the molecules used and in which sub-processes to focus on.

Albeit there is an arguable consensus on the main mechanics of blood vessel growth, different researchers choose different modelling strategies and implementations, resulting in a very diverse spectrum of simulation types. Most teams focus their attention on sprouting angiogenesis, for it is the most researched of the two types of angiogenesis. Nonetheless, even by restraining their focus on a single type of angiogenesis, there are still distinct ways to model this routine. Usually, the different approaches can be divided in cell based models, population based models and, more recently, hybrid models [12].

In cell based models a microscopic view is taken. Each cell is modelled individually and for every cell many interactions and rules have to be expressed. Obviously, this incurs a massive overhead on calculation as the system increases in size and complexity, as is the case when more processes and interactions are added. Moreover, with increasing number of rules and parameters the system becomes progressively more sensitive and harder to control, as even the tiniest of modifications may cause global alterations. Most of these parameters must be observed experimentally, which poses another difficulty, as their measurement is sometimes impossible due to biological constraints (i.e. measure *in vivo* parameters). Thus, they are usually postulated in a way that allows the system to converge and be well-behaved.

The macroscopic approach usually deals with tissue, hence it deals with cell population instead of single cell interaction. They use average concentration or density of endothelial cells and use diffusion equations to model their movement and interaction dynamics. Their capability of inferring about the topology of the structures modelled is limited; they are unable to accurately model vessel branching or overall vascular mesh.

As of late, some researchers have combined both types of models that describe the system in both microscopic and macroscopic views [20,31]. These types of models describe the bulk of the angiogenic process as a tissue, but track and cover the dynamics of some important cells. In blood vessel proliferation, tip cells are pivotal and, as such, their interactions and influences feedback on the entire system. Promptly it can be noticed that this type of hybrid model has a lower computational overhead, as it deals with the population dynamics instead of single cell interactions, consequently having fewer rules and parameters. However, it is capable of predicting resulting capillary networks, through the modelling of tip cells analogously to the microscopic type models. Hence, it can incorporate routines occurring at the cellular and tissue level. In theory, this approach combines the best components of both types of models.

Even though many approaches were taken to tackle this modelling problem, only a scant amount account for the mechanical traits of the system studied, namely the blood vessels and the surrounding medium. This leads to an area that needs enlightenment, as we do not understand or are able to predict how the mechanic signals influence vessel growth. Some authors infer greater importance to the inclusion of mechanical characteristics, as angiogenesis occurs in a mechanically dynamic environment [26,28].

Our model is inserted in this specific area: a continuum model of blood vessel growth that takes into account the system's mechanical characteristics.

Model Development

2.1 Background

The idea of modelling angiogenesis with phase-field is fundamentally based on its simplicity in treating relatively complex systems. In our case, instead of dealing with every cell and their interactions to neighbour cells, which would have a tremendous computational overhead with increasing cell population, we study the shape of the cell population as a whole. This way, we can use simple differential equations to model their dynamics and not worry with case by case effects and interactions, while still being able to track individual cells.

To immerse ourselves in these types of models, the first goal was to effectively model and comprehend phase separation. In order to accomplish this, we begun by modelling a system's evolution based on a notorious[17,34] fourth order, parabolic partial differential equation - the Cahn-Hilliard equation.

The Cahn-Hilliard equation describes phase separation of binary fluids. These fluids have two distinct domains or phases; the result of applying the Cahn-Hilliard equation is a system where both phases are clearly separated and pure (i.e. same value inside their domains). This equation is normally formulated in order to the fluid's concentration; however, it can be rewritten as depending on an order parameter, ϕ. Hence, the Cahn-Hilliard equation can be written as:

$$\frac{\partial \phi}{\partial t} = D\nabla^2 \left(\phi^3 - \phi - \nabla^2 \phi\right) \tag{2.1}$$

where D is a diffusion coefficient.

As we are dealing with cells, D is usually replaced with M, which stands for mobility and is always positive. This is a simple change in formalism, as cell diffusion is not a logic parameter in this subject matter. As such, in this analogue we will always be talking about cell mobility.

This equation is the result of minimizing the system's energy functional. The system's dynamics can be represented by the energy it costs to be in a certain state. This energy cost is a scalar value that depends on the system's state. This state, in turn, depends on the order parameter field $\phi(\mathbf{r}, t)$, so the term energy functional arises. Physically, this free energy functional is dissipative[34], so the system is expected to evolve in such a way that it minimises the total energy, moving from a higher energy level to a lower level.

In the CH case, we begin from the Ginzburg-Landau free energy functional:

$$F[\phi] = \int \mathrm{d}\mathbf{r} \left[f_0(\phi) + \frac{\gamma}{2} (\nabla \phi)^2 \right] \tag{2.2}$$

where $f_0(\phi)$ is the free energy density that in this case is given by:

$$f_0(\phi) = \frac{\phi^4}{4} - \frac{\phi^2}{2} \tag{2.3}$$

replacing (2.3) on (2.2) we get:

$$F[\phi] = \int \mathrm{d}\mathbf{r} \left[\frac{\phi^4}{4} - \frac{\phi^2}{2} + \frac{\gamma}{2}|\nabla\phi|^2 \right] \tag{2.4}$$

The free energy density $f_0(\phi)$ can be manipulated into giving us different values for the phases' domains. This is accomplished by a simple alteration of the function in (2.3)[24]. In this case, as we want to minimise the free energy functional, we will use:

$$\frac{df}{d\phi} = 0 \tag{2.5}$$

which gives:

$$\phi = -1 \vee \phi = 0 \vee \phi = 1 \tag{2.6}$$

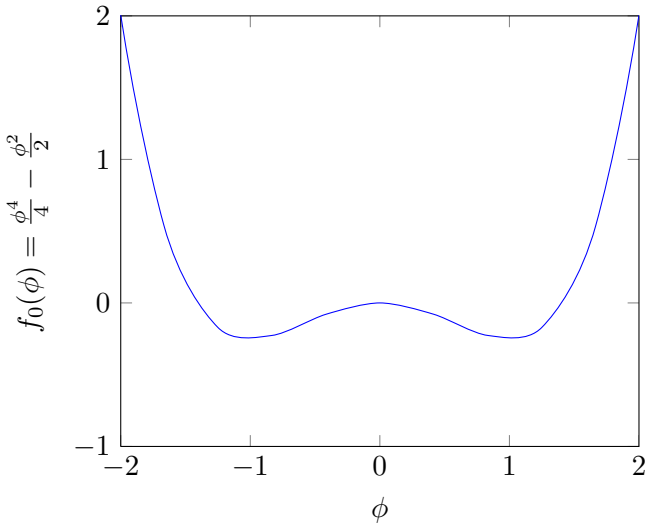

Figure 2.1: Double well shape of $f_0(\phi)$ to clarify the global minima at points $\phi = -1$ and $\phi = 1$.

Of these values, $\phi = 1$ and $\phi = -1$ represent the global minima of the function (which is better illustrated in figure 2.1) and, as such, they are the values corresponding to the two pure phases.

The remaining term on (2.2), $\frac{\gamma}{2}|\nabla\phi|^2$, incurs a penalty for non-optimum interfaces, forcing the surface interface's perimeter to be minimised. This arises from the gradient of ϕ being highest at the interface between the two phases, because it bridges the two values of the domains (i.e. $\phi = 1$ and $\phi = -1$). It follows that a larger interface surface would contribute a bigger term to the energy functional, which is the opposite of our objective: minimise (2.2).

Calculating this functional's derivative systematically:

$$\delta F = F[\phi + \delta\phi] - F[\phi] \tag{2.7}$$

$$F[\phi + \delta\phi] = \int \mathrm{d}\mathbf{r} \left[\frac{(\phi + \delta\phi)^4}{4} - \frac{(\phi + \delta\phi)^2}{2} + \mu_0 + \frac{\gamma}{2}(\nabla(\phi + \delta\phi))^2 \right]$$

eliminating terms higher than $\delta\phi$ because of their insignificant contribution and using the gradient's linearity:

$$\begin{aligned}
&= \int \mathrm{d}\mathbf{r} \left[\frac{\phi^4 + 4\phi^3\delta\phi}{4} - \frac{\phi^2 - 2\phi\,\delta\phi}{2} + \mu_0 + \frac{\gamma}{2}\left((\nabla\phi)^2 + 2(\nabla\phi.\nabla\delta\phi)\right) \right] \\
&= \int \mathrm{d}\mathbf{r} \left[\frac{\phi^4}{4} - \frac{\phi^2}{2} + \mu_0 + \frac{\gamma}{2}(\nabla\phi)^2 + \phi^3\delta\phi + \gamma(\nabla\phi.\nabla\delta\phi) \right] \\
&= F[\phi] + \int \mathrm{d}\mathbf{r} \left[\phi^3\delta\phi - \phi\,\delta\phi + \gamma\,(\nabla\phi.\nabla\delta\phi) \right]
\end{aligned}$$

integrating by parts with periodic boundary conditions the last term:

$$\begin{aligned}
F[\phi + \delta\phi] - F[\phi] &= \int \mathrm{d}\mathbf{r} \left[\phi^3\delta\phi - \phi\,\delta\phi \right] - \int \mathrm{d}\mathbf{r} \left[\gamma\,\delta\phi\,\nabla^2\phi \right] \\
\delta F &= \int \mathrm{d}\mathbf{r} \left[\phi^3 - \phi - \gamma\,\nabla^2\phi \right] \delta\phi \\
\frac{\delta F}{\delta\phi} &= \phi^3 - \phi - \gamma\,\nabla^2\phi \qquad (2.8)
\end{aligned}$$

However, because we want to manipulate the time evolution of the order parameter map (i.e. ϕ) and it is a conserved quantity in our system, we use the canonical continuity equation:

$$\frac{\partial\phi}{\partial t} = -\nabla.\mathbf{j} \tag{2.9}$$

where $\mathbf{j}$ is the concentration flux, which is proportional to the chemical potential in this manner:

$$\mathbf{j} = D(-\nabla\mu) \tag{2.10}$$

and μ is the chemical potential, which quantifies how the energy changes when the particles change position, thus having the following formulation:

$$\mu = \frac{\delta F}{\delta\phi} \tag{2.11}$$

combining (2.11) with (2.9) and (2.10) results in:

$$\frac{\partial\phi}{\partial t} = D\nabla^2\frac{\delta F}{\delta\phi} \tag{2.12}$$

replacing with the derivate we calculated in (2.8)

$$\frac{\partial\phi}{\partial t} = D\nabla^2\left(\phi^3 - \phi - \gamma\,\nabla^2\phi\right) \tag{2.13}$$

It can easily be seen that the last equality, (2.13), is identical to (2.1), as we wanted to prove. Also, consider that these equations force the order parameter ϕ to be conserved as its evolution follows the continuity equation (2.9). Hence, the mean value of the order parameter $\bar{\phi}$ remains the same throughout the simulation.

Simulation wise, we have a two dimensional, lattice (i.e. grid) map that holds the values of an order parameter that distinguishes the two phases of the system for every point in its surface. Simultaneously, we use a partial differential equation to describe the temporal and spacial evolution of the order domains (i.e. their dynamics).

At each iteration, both elements repeatedly supply information to the other; the continuous equation gives the next iteration's value, which is then replaced in the lattice map. Noticeably, the mapping takes continuous information and stores only discrete steps of this data, which is inevitable, due to its lattice nature.

This gives rise to an easily implementable model which is highly modular; starting conditions can be promptly swapped by changing the initial mesh while dynamics can be altered by changing the governing equations or parameters.

We opted for periodic boundary conditions in this test. With this type of boundaries, the neighbour of a point at the boundary is at the opposite boundary.

A useful notion arises by noticing that there is a single solution to the CH equation for a given initial data[34]. Therefore, using the same starting lattice map with equal initial conditions returns the same result. So, despite the stochastic nature of the initial values, the result at each iteration is completely deterministic and given by (2.13). We took advantage of this feature, both here and in later cases, to investigate the influence of changing simulation parameters (e.g. the diffusion constant). Obviously, differences in the two runs that differ by a parameter can only be accounted by the altered parameter itself.

It is evident that, in order to calculate derivatives, the equations need information that is obtained from the surrounding area. In the continuous case this is trivial, however, the mesh stores only discrete samples of values, sampled from the continuous case with a spacing h. Hence, an approximation was needed. For this purpose, (2.13) was approximated using the finite differences method, resulting in this formulation:

$$\frac{\phi_{i,j}^{n+1} - \phi_{i,j}^{n}}{\Delta t} = D\nabla^2 \left(\phi_{i,j}^3 - \phi_{i,j} - \gamma\nabla^2\phi_{i,j}\right)$$
$$\phi_{i,j}^{n+1} = \phi_{i,j}^{n} + \Delta t\, D\, \nabla^2 \left(\phi_{i,j}^3 - \phi_{i,j} - \gamma\nabla^2\phi_{i,j}\right)$$

In the above equation Δt is the step size used in the approximation. This step size was chosen to be as close to the threshold for stability as possible in order to have a fast enough simulation. We used for this simulation $\Delta t = 0.02$ and $D = 1$. We will use these values constantly throughout the development, as such, they will be omitted in simulation descriptions.

In addition, by using finite differences approximation on the Laplace operator ∇^2, we get:

$$\begin{aligned}\nabla^2\phi_{i,j} &= \frac{\partial^2\phi_{i,j}}{\partial x^2} + \frac{\partial^2\phi_{i,j}}{\partial y^2} \\ &\simeq \frac{\phi_{i-h,j} - 2\phi_{i,j} + \phi_{i+h,j}}{h^2} + \frac{\phi_{i,j-h} - 2\phi_{i,j} + \phi_{i,j+h}}{h^2} \\ &\simeq \frac{\phi_{i-h,j} + \phi_{i+h,j} + \phi_{i,j-h} + \phi_{i,j+h} - 4\phi_{i,j}}{h^2}\end{aligned}$$

because we are in a unit lattice mesh we will use $h = 1$ as the spacing, resulting in:

$$\nabla^2\phi_{i,j} \simeq \phi_{i-1,j} + \phi_{i+1,j} + \phi_{i,j-1} + \phi_{i,j+1} - 4\phi_{i,j}$$

For the initial conditions in this test, we chose the most usually used in a simulation environment: superimposing a random noise component on a predefined average value inside the spinodal region[4].

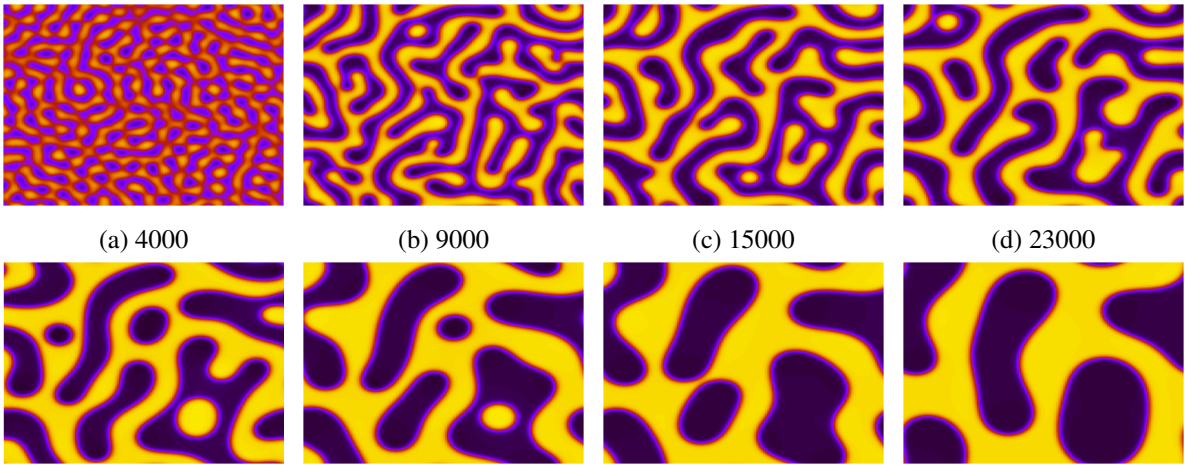

(a) 4000 (b) 9000 (c) 15000 (d) 23000

(e) 45000 (f) 90000 (g) 140000 (h) 250000

Figure 2.2: Simulation on a 128 lattice square mesh of the Cahn-Hilliard equation with $\Delta t = 0.02$ and average order $\bar{\phi} = 0$. Below each image is the iteration number.

Usually, only a small random perturbation around the average value is necessary. In our case, we used gcc's* built-in pseudo-random number generator to populate the mesh with a distribution of values in the $[-0.005 : 0.005]$ range. In this range, the average order value is null, as, in principle, there is equal probability of each point having $\phi < 0$ or $\phi > 0$, thus, in average $\bar{\phi} = 0$.

In these results several properties of spinodal decomposition can be observed. From a disordered initial state, we see, very early in the simulation, the formation of ordered domains with well defined order parameter ϕ values. This arises directly from particles of the same type reorganizing themselves spatially to minimise the system's enthalpy. Thus, interactions between particles of the same type are favourable, while interactions between different types of particles are unfavourable.

A curious phenomenon that can also be observed in figure 2.2 is the disappearing of small domains by adding their material to the larger domains. This is called *Ostwald Ripening*[27]. In this situation, it is a

*`http://gcc.gnu.org/`

consequence of the interface minimization term we added to the free energy, that represents the concept that molecules on the surface of a particle are energetically less stable than those in the interior. According to the Kelvin equation[†], the unstable molecules on the surface of a small particle will detach themselves and diffuse into the medium. When saturated, these free molecules usually condense on the surface of the larger particles. Moreover, if a phase is more abundant than the other, this phenomenon is more likely to happen.

In the end, the system converges to a solution that consists of mostly large spherical domains. This tendency can be partially observed in the last images of figure 2.2.

This test was a good starting point to understand and gain experience in modelling simple phase field models and to study their computational efficiency. This simulation's script allowed experimentations on modularity of the program for use as a stub or skeleton for later models.

[†]This equation's formulation and a more detailed discussion are in appendix A

2.2 Including Elasticity in Phase-field

We will start by reformulating our free-energy functional to include a term of elastic energy. This term has the following canonical form:

$$f_{el}(\epsilon_{ij}) = \lambda \left(\sum_{i}^{2} \epsilon_{ii} \right)^2 + 2\mu \sum_{i}^{2} \sum_{j}^{2} \epsilon_{ij}^2 \tag{2.14}$$

where λ is the first Lamé parameter, μ is the shear modulus and ϵ_{ij} is the strain tensor given by:

$$\epsilon_{ij} = \frac{1}{2}(\partial_i u_j + \partial_j u_i) \tag{2.15}$$

in which $\mathbf{u}$ is the displacement vector.

Our interest is in the volume dilation and shear characteristics. For this purpose, we will rewrite (2.14) in the following way[‡]:

$$f_{el}(\mathbf{u}) = K \left(\nabla.\mathbf{u}\right)^2 + 2\mu \sum_{i,j}^{2} \left(\frac{1}{2}(\partial_i u_j + \partial_j u_i) - \frac{1}{d}\delta_{ij}\nabla.\mathbf{u} \right)^2 \tag{2.16}$$

where K is the bulk modulus and d is the dimension of the system.

We assume that the bulk modulus K is constant throughout the simulation, but that the shear modulus depends on the order parameter is this way:

$$\mu = \mu_0 + \mu_1 \phi \tag{2.17}$$

where $\mu_1 \ll \mu_0$ so that in no instance we have $\mu < 0$.

Because of this term, we quickly cause an asymmetry on the mechanical effects of each of the phases; one is a "soft" phase (i.e. more pliable), whereas the other has greater resistance to these effects – a "hard" phase. We deduce this from the value of μ_1; positive values of ϕ result in a shear modulus that is bigger than μ_0. On the other hand, negative values result in a μ lower than μ_0. In conclusion, negative values of ϕ correspond to a lower shear modulus, thus a "soft" domain, while positive values of ϕ correspond to a "hard" domain. Seeing as after phase separation all values that are not in an interface will belong to the two pure domains, we will have pure hard and soft domains.

Before integrating this new term in the free energy functional, we will add yet another term. This new term arises from the possible differences in isotropic strains of phases with the same elastic moduli. There is a simplified solution to this problem in the form of an empirical rule called Vegard's Law[6]. In its statement, this rule relates concentration change to the spatial distance between unit cells in a lattice. Thus, we can relate volume dilation with the order parameter.

The volume dilation can be given by the trace of the strain tensor, as they are the components of strain in the directions perpendicular to the volume's surface. As such, we can easily see that:

$$Tr(\epsilon_{ij}) = \partial_i u_i = \nabla.\mathbf{u} \tag{2.18}$$

[‡]As described in appendix B

Hence, the term corresponding to the Vegard Law can be written as $\alpha\phi\nabla.\mathbf{u}$, with α as a proportionality constant. Adding this term and the elastic energy (2.14) to the free energy functional (2.2) we get its final formulation:

$$F[\phi,\mathbf{u}] = \int \mathrm{d}\mathbf{r}\left[f_0(\phi) + \frac{\gamma}{2}|\nabla\phi|^2 + \alpha\phi\nabla.\mathbf{u} + f_{el}(\mathbf{u})\right] \tag{2.19}$$

We will now proceed by eliminating the elastic field $\mathbf{u}$ from the functional by using the same method as in (2.7). Eliminating the elastic field is necessary due to the different time scales of the two fields, resulting in much simpler equations.

$$F+\delta F = \int \mathrm{d}\mathbf{r}\left[\alpha\phi\nabla.(\mathbf{u}+\delta\mathbf{u}) + \frac{1}{2}\left(K-\frac{2\mu}{d}\right)\left(\nabla.(\mathbf{u}+\delta\mathbf{u})\right)^2 + \right.$$
$$\left.\frac{\mu}{2}(\partial_j(u_i+\delta u_i)\partial_i(u_j+\delta u_j) + \partial_i(u_j+\delta u_j)\partial_i(u_j+\delta u_j))\right]$$

eliminating terms with order higher that $\delta\mathbf{u}$:

$$\delta F = \int \mathrm{d}\mathbf{r}\left[-\delta\mathbf{u}(\alpha\nabla\phi) - \delta\mathbf{u}\nabla\left[\left(K-\frac{2\mu}{d}\right)\nabla.\mathbf{u}\right] - \delta\mathbf{u}\left(\partial_i\left[\mu\partial_j u_i\right] + \partial_i\left[\mu\partial_i u_j\right]\right)\right]$$
$$-\frac{\delta F}{\delta\mathbf{u}} = \alpha\nabla\phi + \nabla\left[\left(K-\frac{2\mu}{d}\right)\nabla.\mathbf{u}\right] + \partial_i\left[\mu\partial_j u_i\right] + \partial_i\left[\mu\partial_i u_j\right]$$

The elastic relaxation of the system is much faster than the phase dynamics as mentioned before. Therefore, we impose the mechanical equilibrium condition:

$$\frac{\delta F}{\delta\mathbf{u}} = 0 \tag{2.20}$$

The next step is to replace (2.17) and $L_0 = K + \mu_0\left(2-\frac{2}{d}\right)$ in the mechanical equilibrium equation. Because the shear modulus μ has two different components, we will also have $\mathbf{u} = \mathbf{u}^0 + \mathbf{u}^1$ and $\mathbf{u}^0 \gg \mathbf{u}^1$. As the equations are large, we shall divide their derivation into two steps: terms of zeroth-order and first-order.

Consequently, for the zeroth-order:

$$\alpha\nabla\phi + (L_0-\mu_0)\nabla\left(\nabla.\mathbf{u}^0\right) + \mu_0\nabla^2\mathbf{u}^0 = 0$$

taking the divergence of this equation results in:

$$\alpha\nabla^2\phi + (L_0-\mu_0)\nabla^2\left(\nabla.\mathbf{u}^0\right) + \mu_0\nabla^2\left(\nabla.\mathbf{u}^0\right) = 0$$
$$\Leftrightarrow \alpha\nabla^2\phi + L_0\nabla^2\left(\nabla.\mathbf{u}^0\right) = 0$$
$$\Rightarrow \nabla.\mathbf{u}^0 = -\frac{\alpha\phi}{L_0}$$

using a new potential ω that can be derived from $\mathbf{u}^0 = -\frac{\alpha}{L_0}\nabla\omega$, the equation becomes:

$$\nabla^2\omega = \phi \tag{2.21}$$

Notice that this expression is written for when $\bar{\phi} = 0$, i.e. the displacements only occur when the order parameter deviates from the average. In the simulations we present, we subtracted $\bar{\phi}$ from ϕ. For simplicity we will keep deriving the equation with $\bar{\phi} = 0$.

With (2.21) we can now eliminate the elastic field from the equations by substituting them on the free energy equation. We will use the same strategy as above and separate the zeroth and first orders and check their contribution for the final equation individually.

Thus, for the zeroth-order, we have:

$$F^0[\phi, \mathbf{u}] = \int \mathrm{d}\mathbf{r} \left[f_0(\phi) + \alpha\phi\nabla.\mathbf{u} + f_{el}^0 \right] \tag{2.22}$$

using (2.21) and the expansion of f_{el}^0 given on appendix B:

$$\begin{aligned}
F^0[\phi] &= \int \mathrm{d}\mathbf{r} \left[f_0(\phi) - \frac{\alpha^2}{L_0}\phi\nabla^2\omega + \frac{\alpha^2}{2L_0}\phi^2 - \mu_0\frac{\alpha^2}{L_0^2}\phi^2 + \frac{\alpha^2\mu_0}{L_0^2}\partial_{ij}\omega\partial_{ij}\omega \right] \\
&= \int \mathrm{d}\mathbf{r} \left[f_0(\phi) - \frac{\alpha^2\phi^2}{L_0} + \frac{\alpha^2\phi^2}{2L_0} - \frac{\mu_0\alpha^2}{L_0^2}\phi^2 + \frac{\alpha^2\mu_0}{L_0^2}\partial_{ii}\omega\partial_{jj}\omega \right] \\
&= \int \mathrm{d}\mathbf{r} \left[f_0(\phi) - \frac{\alpha^2\phi^2}{2L_0} - \frac{\mu_0\alpha^2}{L_0^2}\phi^2 + \frac{\mu_0\alpha^2}{L_0^2}\phi^2 \right] \\
&= \int \mathrm{d}\mathbf{r} \left[f_0(\phi) - \frac{\alpha^2\phi^2}{2L_0} \right] \\
&= \int \mathrm{d}\mathbf{r} \left[f(\phi) \right] \qquad (2.23)
\end{aligned}$$

The final equation has no dependence on $\mathbf{u}$ as intended. Moreover, this term differs from the Cahn-Hilliard equation by $-\frac{\alpha^2\phi^2}{2L_0}$, which, given suitable values for these parameters, simplifies to a similar equation.

For the term proportional to the first order:

$$F^1[\phi, \mathbf{u}] = \int \mathrm{d}\mathbf{r} \left[\alpha\phi\nabla.\mathbf{u}^1 + f_{el}^1 \right]$$

substituting (2.21) and the expansion of f_{el}^1 that is given on appendix B on this equation, gives:

$$\begin{aligned}
F^1[\phi, \mathbf{u}] = \int \mathrm{d}\mathbf{r} \Bigg[&\alpha\nabla^2\omega\nabla.\mathbf{u}^1 - \frac{K\alpha}{L_0}\nabla^2\omega\nabla.\mathbf{u}^1 + \frac{\mu_1\alpha^2}{L_0^2}\phi\partial_{ij}\omega\partial_{ij}\omega - \\
&\frac{\mu_1\alpha^2\phi}{dL_0^2}(\nabla^2\omega)^2 - \frac{2\alpha\mu_0}{L_0}\partial_{ij}\omega\partial_j u_i^1 + \frac{2\alpha}{dL_0}\mu_0\nabla^2\omega\nabla.\mathbf{u}^1 \Bigg] \\
= \int \mathrm{d}\mathbf{r} \left[-\frac{\alpha}{L_0}\left(-L_0 + K + 2\mu_0 - \frac{2\mu_0}{d} \right)\nabla^2\omega\nabla.\mathbf{u}^1 + \frac{\mu_1\alpha^2}{L_0^2}\phi\partial_{ij}\omega\partial_{ij}\omega - \frac{\alpha^2\mu_1\phi}{dL_0^2}(\nabla^2\omega)^2 \right] \\
\Rightarrow F^1[\phi] = \frac{\mu_1\alpha^2}{L_0^2}\int \mathrm{d}\mathbf{r} \left[\phi\left(\partial_{ij}\omega\partial_{ij}\omega - \frac{1}{d}(\nabla^2\omega)^2 \right) \right]
\end{aligned}$$

completing the squares:

(2.24)
$$F^1[\phi] = \frac{\mu_1 \alpha^2}{L_0^2} \int \mathrm{d}\mathbf{r} \left[\phi \left(\partial_{ij}\omega - \frac{1}{d}\delta_{ij}\nabla^2\omega \right)^2 \right]$$

Ending in another term that has $\mathbf{u}$ eliminated. Putting (2.23) and (2.24) with the remaining term of (2.19) together, will return the final formulation for the free energy functional fully independent of terms proportional to $\mathbf{u}$. Thus:

$$F[\phi] = \int \mathrm{d}\mathbf{r} \left[f(\phi) + \frac{\gamma}{2}(\nabla\phi)^2 + \frac{\mu_1 \alpha^2}{L_0^2} \phi \left(\partial_{ij}\omega - \frac{1}{d}\delta_{ij}\nabla^2\omega \right)^2 \right]$$

or more compactly:

$$F[\phi] = \int \mathrm{d}\mathbf{r} \left[f(\phi) + \frac{\gamma}{2}(\nabla\phi)^2 + \frac{\mu_1 \alpha^2}{L_0^2} \phi Q \right]$$

with $Q = \left(\partial_{ij}\omega - \frac{1}{d}\delta_{ij}\nabla^2\omega \right)^2$.

As before, we want to study the temporal and spatial evolution of the order parameter. Using the same type of equation as (2.12) leaves us with the task of calculating $\frac{\delta F}{\delta \phi}$. As the first two terms have similar derivations to the Cahn-Hilliard solution, only the third term will be computed in the following:

$$\begin{aligned}
\delta F_{el} &= \int \mathrm{d}\mathbf{r} \frac{\alpha^2}{L_0^2} \left[\mu_1 Q \delta\phi + 2\mu_1 \phi \left(\partial_{ij}\delta\omega - \frac{1}{d}\delta_{ij}\nabla^2\delta\omega \right) \left(\partial_{ij}\omega - \frac{1}{d}\delta_{ij}\nabla^2\omega \right) \right] \\
&= \int \mathrm{d}\mathbf{r} \frac{\alpha^2}{L_0^2} \left[\mu_1 Q \delta\phi + 2\mu_1 \phi \left(\partial_{ij} \left[\frac{1}{\nabla^2} \right] \delta\phi - \frac{1}{d}\delta_{ij}\delta\phi \right) \left(\partial_{ij}\omega - \frac{1}{d}\delta_{ij}\nabla^2\omega \right) \right] \\
&= \int \mathrm{d}\mathbf{r} \frac{\alpha^2}{L_0^2} \left[\mu_1 Q \delta\phi + 2\mu_1 \phi \left(\partial_{ij}\omega - \frac{1}{d}\delta_{ij}\nabla^2\omega \right) \partial_{ij} \left[\frac{1}{\nabla^2} \right] \delta\phi - \right. \\
&\qquad \left. 2\mu_1 \phi \left(\partial_{ij}\omega - \frac{1}{d}\delta_{ij}\nabla^2\omega \right) \frac{1}{d}\delta_{ij}\delta\phi \right] \\
&= \int \mathrm{d}\mathbf{r} \frac{\alpha^2}{L_0^2} \left[\mu_1 Q \delta\phi + 2\mu_1 \phi \left(\partial_{ij}\omega - \frac{1}{d}\delta_{ij}\nabla^2\omega \right) \partial_{ij} \left[\frac{1}{\nabla^2} \right] \delta\phi \right] \\
&= \int \mathrm{d}\mathbf{r} \frac{\alpha^2}{L_0^2} \left[\mu_1 Q \delta\phi + 2\mu_1 \partial_{ij} \left[\frac{1}{\nabla^2} \right] \left\{ \phi \left(\partial_{ij}\omega - \frac{1}{d}\delta_{ij}\nabla^2\omega \right) \right\} \delta\phi \right] \\
\frac{\delta F_{el}}{\delta \phi} &= \frac{\alpha^2 \mu_1}{L_0^2} Q + 2\frac{\alpha^2 \mu_1}{L_0^2} \partial_{ij} \left[\frac{1}{\nabla^2} \right] \left\{ \phi \left(\partial_{ij}\omega - \frac{1}{d}\delta_{ij}\nabla^2\omega \right) \right\}
\end{aligned}$$

Adding this term with (2.8) and replacing it in (2.12) returns the dynamic equation of the system's evolution. We now replace μ_1 by g_E, with $g_E = \mu_1 \alpha^2 / L_0^2$, emphasising its importance in weighing the effect of the elastic terms:

$$\frac{\partial \phi}{\partial t} = \nabla^2 \left[\phi^3 - \phi - \nabla^2 \phi + g_E\, Q\right] + 2 g_E \sum_{i,j} \partial_{ij} \left\{ \phi \left[\partial_{ij}\, \omega - \frac{1}{d}\, \delta_{ij} \nabla^2 \omega \right] \right\} \tag{2.25}$$

We started simulation of these equations with the initial availability of each type of material biased, in this case towards making hard material predominant. To this effect, the initial mesh had an average value of 0.2 for the order parameter, with pseudo-random noise added with values in the range $[-0.001; 0.001]$. This way, by averaging all values of the order parameter we would have, ideally, $\bar{\phi}_0 = 0.2$.

This model was extensively simulated with different arrangements of the available factors and compared against the previously mentioned literature. The results were similar, so both the modelling procedure and the equations used were proven correctly implemented.

An interesting and important parameter in this step of modelling is the elastic prevalence g_E. This factor is responsible for the influence that the elastic terms have on each step of the system's evolution. It is directly observable from equation (2.25) that with $g_E = 0$, it would become:

$$\frac{\partial \phi}{\partial t} = \nabla^2 \left[\phi^3 - \phi - \nabla^2 \phi\right] \tag{2.26}$$

which is (2.1), the Cahn-Hilliard equation. Hence, a very low g_E value will result in results very similar to the ones given by the CH equation.

Comparing the results obtained with having changed only g_E, we can see that for both values of g_E the system follows the usual steps of phase separation by creating two distinct domains. However, very early in the simulation with a high value of g_E (figure 2.4), the soft material (in black/blue) deforms itself to bridge same value domains, while in the case with a low value of g_E (figure 2.3) formation of round, separate domains (i.e. droplets) is more common.

Thus, when we increase the prevalence of elasticity by increasing the value of g_E, the system's soft domains are more flexible and tend to bridge close phases of the same type (i.e. percolation). This also influences the probability of *Ostwald Ripening* happening, which becomes less likely as even small domains can be bridged and not just have their material slowly incorporated into larger domains (even on a system with more soft-phase available initially). However, when we decrease the value of g_E the formation of droplets, which will later incorporate more material or be incorporated, is more prevalent.

Another fundamental concept of these equations is the role of ω, as it is used in every elastic term of (2.25). Due to the sequence in computation, the values of the ω map can be used to predict the values of the ϕ mesh. Moreover, the sign of its value is always opposite to the corresponding value on ϕ; if $\omega < 0$ then $\phi > 0$ and vice-versa.

Both these characteristics are important to know beforehand the sign of any modification or perturbation of mechanical nature we want to cause on the order map, because we would have to change the elastic terms which are mostly represented by ω. These features will be used for this very purpose on the next section (2.3).

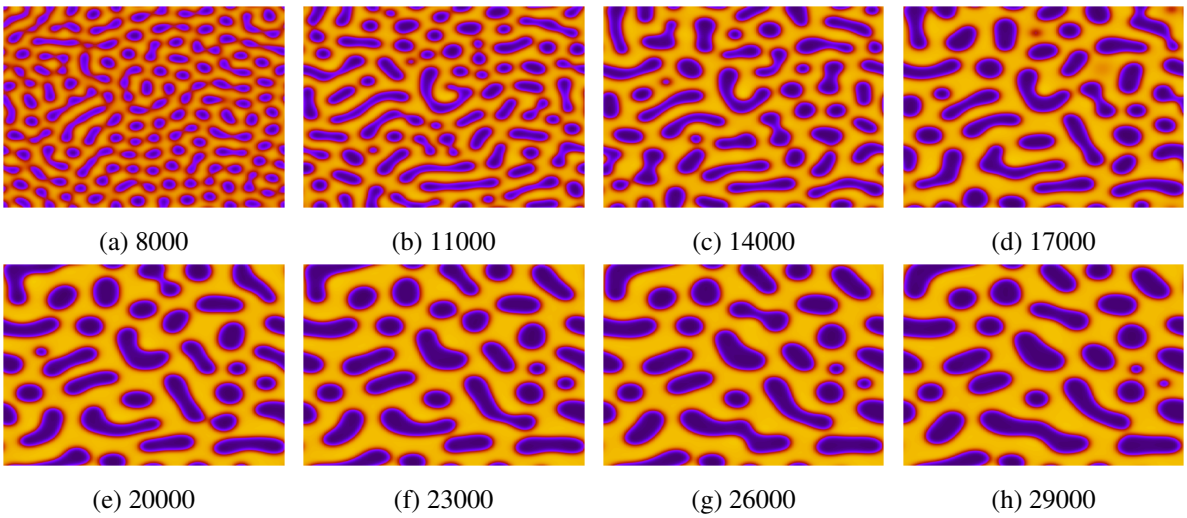

(a) 8000 (b) 11000 (c) 14000 (d) 17000

(e) 20000 (f) 23000 (g) 26000 (h) 29000

Figure 2.3: Simulation on a 128 by 128 lattice mesh of the evolution of ϕ with $g_E = 0.02$ and $\bar{\phi}_0 = 0.2$. Formation of droplets of soft-phase (in blue/black) over a hard domain (yellow/orange) are observable.

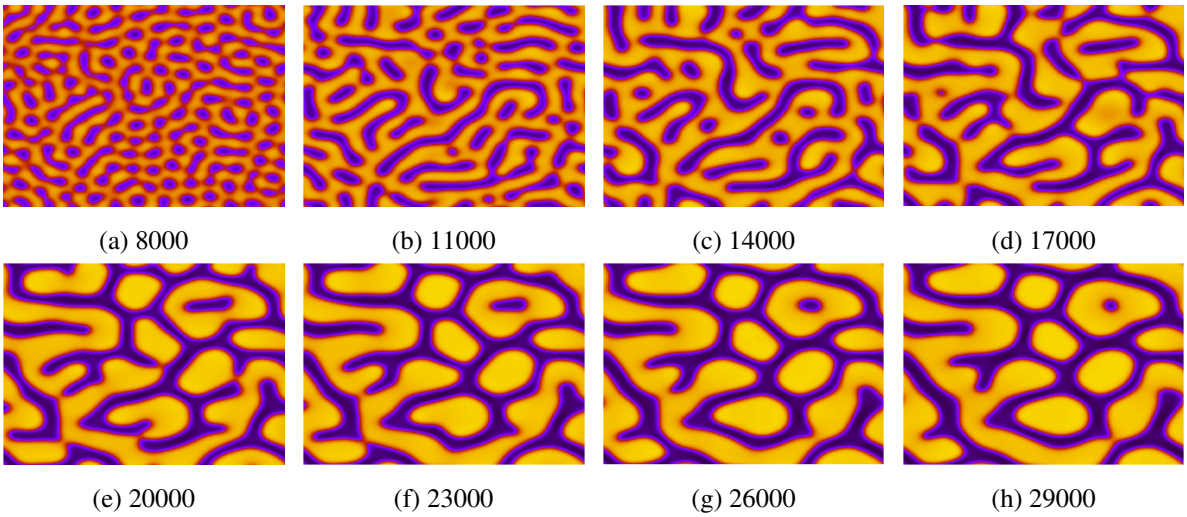

(a) 8000 (b) 11000 (c) 14000 (d) 17000

(e) 20000 (f) 23000 (g) 26000 (h) 29000

Figure 2.4: Simulation on a 128 by 128 lattice mesh of the evolution of ϕ with $g_E = 0.10$ and $\bar{\phi}_0 = 0.2$. Notice the network of interconnected soft-phases (in blue/black) formed over the hard-phases (yellow/orange).

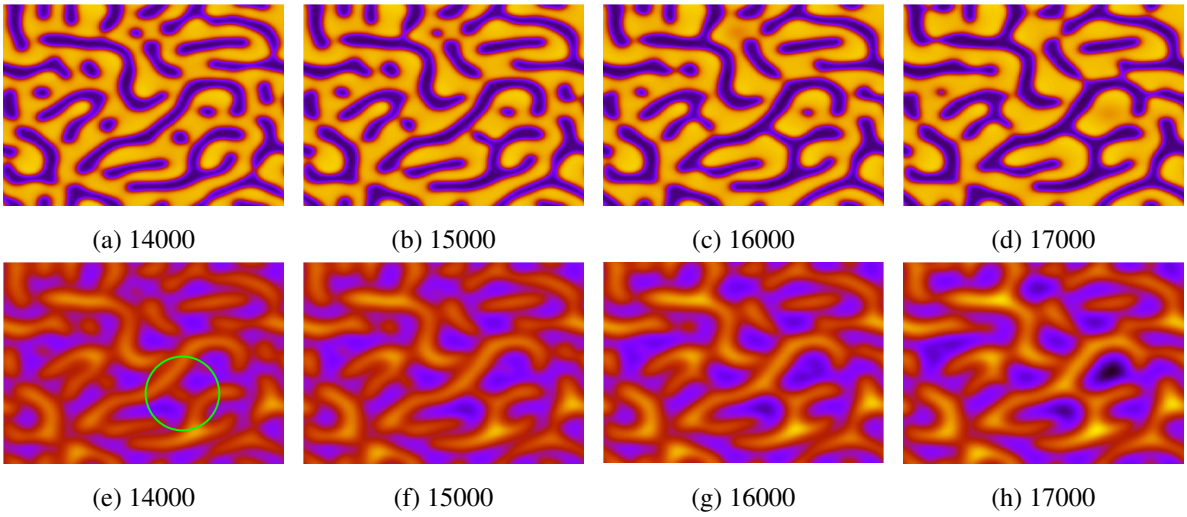

(a) 14000 (b) 15000 (c) 16000 (d) 17000

(e) 14000 (f) 15000 (g) 16000 (h) 17000

Figure 2.5: Simulation of the evolution of ϕ (from (a) to (d)) and ω (from (e) to (h)) with $g_E = 0.10$ and $\bar{\phi}_0 = 0.2$ with iteration numbers below each image. On both maps, blue/black is negative and red/orange positive, so it is easy to notice the opposite sign, but similar shape between the two maps. Also, note the phase bridging (highlighted green in (e)) that occurs in ω many iterations before it happens in ϕ .

2.3 First Steps towards Cell Migration

The next step was to include a way to effectively control forces used in the system. This step was crucial in developing a model that was capable of emulating cell migration with accurate tensile effects. In a physical perspective, the movement of the tip cell can be understood as a compressive force centred on the interface between cell membrane and ECM. Consider the movement along an axis, with the forward direction (i.e. direction of migration) being positive. Then, the cell's pulling on the ECM can be represented by a force applied on the ECM adjacently to the interface. This force will have a direction opposite to the migration and, thus, will be *negative*. Subsequently, a force with equal magnitude, will be applied on the vessel, close to the interface, with the same direction as the migration, hence *positive*.

By using these two forces to create a compressive influence at the interface, it would be expected that the net movement would be zero. However, considering the rigid characteristics of the structure being pulled (the ECM), only the cell will have significant net movement; in this case, in the forward direction.

This concept is better elucidated in figure 2.7 and the shape of the force described is illustrated in figure 2.6.

The suggested topology for the force is in accordance to the physics explained above. Hence, for the problem at hand, it was surmised that the above curve would shape the surface of the force in the migration direction, and that its effect would decay exponentially in the perpendicular direction.

To create a function that would have these characteristics, a piecewise function could be constructed. However, a much simpler approach was taken: we used the directional derivative along the migration vector of a standard Gaussian function. The resulting function's shape has the chosen characteristics and can be easily manipulated in both amplitude and radius. These features make it the best choice for this

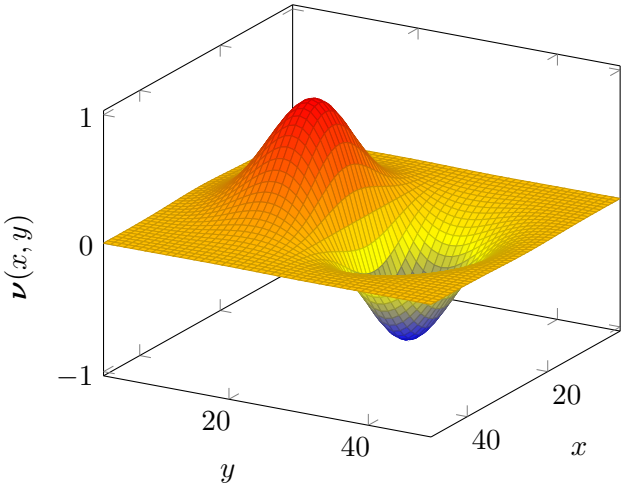

Figure 2.6: Topology of the force field $\boldsymbol{\nu}(x, y)$ created to mimic cellular movement; in this case the cell is moving in the y direction.

simulation, as different radii of effect will need to be used. Moreover, the force's effect is not constant in every step of the migration, so by adjusting the function's amplitude, we can control the force's strength on the intervening subsystem.

Accordingly, we have the following formulation for the force field, which we termed $\boldsymbol{\nu}$:

$$\begin{aligned} \boldsymbol{\nu} &= \nu_x \hat{\imath} + \nu_y \hat{\jmath} \\ &= \nabla_{\mathbf{u}} f(x, y) \\ &= (\nabla f(x, y).\mathbf{u})\,\mathbf{u} \end{aligned} \tag{2.27}$$

where $\mathbf{u}$ is the unit vector that corresponds to the direction of migration and $f(x, y)$ is just the standard gaussian function given by:

$$f(x, y) = e^{-\frac{(x-x_0)^2+(y-y_0)^2}{2\sigma_x\sigma_y}}$$

with center $C = \{x_0, y_0\}$ and radii σ_x and σ_y.

Note that (2.27) was chosen purely for computational purposes, as the point gradient is easily calculated with finite differences and multiplication with vector $\mathbf{u}$ is simple. To include this new force field, the mechanical equilibrium equation (2.20) had to be rewritten to include the force field $\boldsymbol{\nu}$ (i.e. our interference):

$$\frac{\delta F}{\delta \mathbf{u}} = S\boldsymbol{\nu}$$

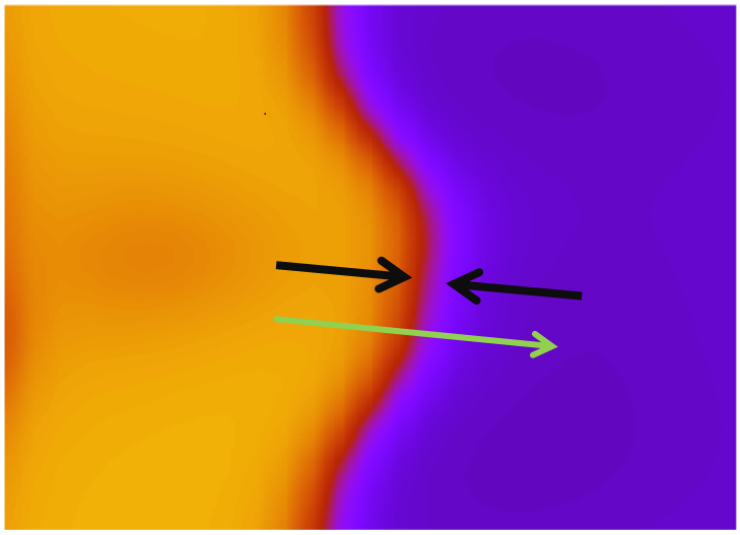

Figure 2.7: Scheme representing the direction of forces (in black) individually applied to the ECM (blue domain) and vessel (yellow domain) to create a compressive effect on the interface. Net movement is in the direction of migration and is represented in green.

The factor S above is the force's amplitude. The consequences in the prior equations follow:

$$\begin{aligned}
&\alpha\nabla\phi + (L_0 - \mu_0)\,\nabla\left(\nabla.\boldsymbol{u}^0\right) + \mu_0\nabla^2\boldsymbol{u}^0 = -S\boldsymbol{\nu} \\
\Rightarrow\ &\alpha\nabla^2\phi + (L_0 - \mu_0)\,\nabla^2\left(\nabla.\boldsymbol{u}^0\right) + \mu_0\nabla^2\left(\nabla.\boldsymbol{u}^0\right) = -S\nabla.\left(\boldsymbol{\nu}\right) \\
\Leftrightarrow\ &\alpha\nabla^2\phi + L_0\nabla^2\left(\nabla.\boldsymbol{u}^0\right) - \mu_0\nabla^2\left(\nabla.\boldsymbol{u}^0\right) + \mu_0\nabla^2\left(\nabla.\boldsymbol{u}^0\right) = -S\nabla.\left(\boldsymbol{\nu}\right) \\
\Leftrightarrow\ &\nabla^2\left(\alpha\phi + L_0\nabla.\boldsymbol{u}^0\right) = -\nabla.\left(S\boldsymbol{\nu}\right) \\
\Leftrightarrow\ &\nabla.\boldsymbol{u}^0 = -\frac{S}{L_0}\left[\frac{1}{\nabla^2}\right]\nabla.\boldsymbol{\nu} - \frac{\alpha\phi}{L_0} \\
\Rightarrow\ &\nabla^2\omega = K\left[\frac{1}{\nabla^2}\right]\nabla.\boldsymbol{\nu} + \left(\phi - \bar{\phi}\right)
\end{aligned}$$

where K is just $\frac{L_0 S}{\alpha}$, which is the interference's amplitude and where in the last line we present the equation used in the code, which is the adimensional version.

With these changes, we get a new formulation for ω. To simplify the last equation, we define:

$$\begin{aligned}
\nabla^2\chi &= \nabla.\boldsymbol{\nu} \\
\chi &= \left[\frac{1}{\nabla^2}\right]\nabla.\boldsymbol{\nu}
\end{aligned}$$

Replacing χ on the same equation yields the much simpler:

$$\nabla^2\omega = \phi - \bar{\phi} + K\chi \tag{2.28}$$

The effect of $\boldsymbol{\nu}$ on the system is represented by χ. Hence, it is its shape that will effectively increase or decrease the values in the area of the order map that the interference is applied.

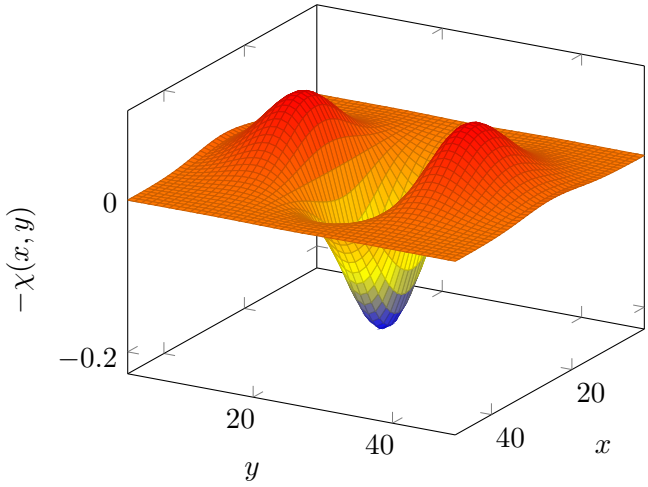

Figure 2.8: Topology of $\chi(x, y)$ that results from equation (2.3).

With the adapted equations, by creating a force field $\boldsymbol{\nu}$ centred on a chosen interface, a protrusion could be created in such a way that it could bridge two different interfaces. The interface point would emulate the tip cell scenario of sprouting angiogenic growth. However, as it is a *single* cell perceiving the environment, its receptive scope for cues is quite limited. This is in accordance to the real case, where the location of the tip cell is one of the determinant factors that influences the direction it will follow. Additionally, every part of the front of the protrusion can act as a tip cell, it only depends on where in the interface the force is applied.

As the tip cell analogue, it also has the responsibility of emulating the gripping on the ECM to pull on it to move it and the trailing part of the sprout forward. Accordingly, the interface closest to it in the direction of migration will become the center of $\boldsymbol{\nu}$ at each pulling event.

An algorithm was devised to find a point belonging to the interface, so that the tip cell concept could be fully tested:

1. An initial point is chosen (it can be random or close to a desired interface);

2. The neighbourhood is probed radially according to Chebychev metric;

3. If a point with ϕ in the $[-0.4 : 0.4]$ range is found, it is declared an interface point.

The Chebychev distance between points p and q, with coordinates p_i and q_i, is defined as:

$$D_{Chebychev}(p, q) := max_i(|p_i - q_i|)$$

Our use of Chebychev metric rests on its easy implementation and because in one iteration it reaches all its adjacent neighbours.

The choice for the interval used in the algorithm results from knowing that both phases' values are very close to $\phi = 1$ or $\phi = -1$. Therefore, any value sufficiently far from these values belongs to the steep slope between phases.

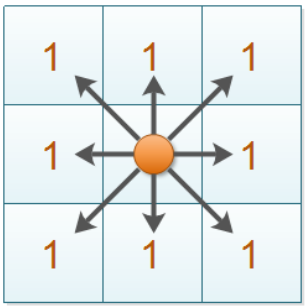

Figure 2.9: Diagram showing the Chebychev distance between the middle cell and each of its eight adjacent cells.

Notice that the mean value could not be used directly to search for interfaces, as is usually the case in phase field models. This is caused by the integer nature of the mesh (i.e. undershoot and overshoot of the theoretical value on the interface). One alternative would be to interpolate the values on the interface, but it would result in an arguable computation waste. In addition, calculating the gradient on the starter point could be a possibility, however it would just return the direction of the interface, creating an unnecessary and unhelpful step on the interface-finding algorithm.

Upon finding the interface, it was necessary to choose a direction in which to migrate. In this stage, we used a direction normal to the interface. This would prove to be useful for later steps in the model, as the method for calculating the interfacial point would remain the same. To calculate a direction normal to the surface of the interface, we computed the gradient at the point found in the interface. For this purpose, a finite difference method was chosen. Hence, the gradient at interfacial point I is:

$\nabla\phi_{x,y}$ at I:

$$\nabla\phi_{x_I,y_I} = \frac{\partial\phi_{x_I,y_I}}{\partial x}\hat{\imath} + \frac{\partial\phi_{x_I,y_I}}{\partial y}\hat{\jmath}$$

using finite differences approximation, we can rewrite as:

$$\nabla\phi_{x_I,y_I} \simeq \frac{\phi_{x_I+1,y_I} - \phi_{x_I-1,y_I}}{2}\hat{\imath} + \frac{\phi_{x_I,y_I+1} - \phi_{x_I,y_I-1}}{2}\hat{\jmath}$$

This calculated gradient will form the components of the direction vector $\boldsymbol{\nu}$ used above. Reformulating the equations to reflect this change in notation:

$$u_x = \frac{\phi_{x_I+1,y_I} - \phi_{x_I-1,y_I}}{2}$$
$$u_y = \frac{\phi_{x_I,y_I+1} - \phi_{x_I,y_I-1}}{2}$$

It is then normalised by dividing by its norm, to get its direction:

$$u_x \simeq \frac{u_x}{\|u\|}$$
$$u_y \simeq \frac{u_y}{\|u\|}$$
$$\text{where } \|\mathbf{u}\| = \sqrt{u_x^2 + u_y^2}$$

This value is then used to calculate the final form of the compressive force, which will be centred in point I. Starting from the formulation given above:

$$\begin{aligned}\boldsymbol{\nu} &= [\nabla f_{x,y}.\mathbf{u}]\,\mathbf{u} \\ &= \left[\left(\frac{\partial f}{\partial x}\hat{\imath} + \frac{\partial f}{\partial y}\hat{\jmath}\right).(u_x\hat{\imath} + u_y\hat{\jmath})\right](u_x\hat{\imath} + u_y\hat{\jmath})\end{aligned}$$

converting it to a finite difference formulation yields:

$$\nu_{x,y} \simeq \left(u_x\frac{f_{x+1,y} - f_{x-1,y}}{2} + u_y\frac{f_{x,y+1} - f_{x,y-1}}{2}\right)(u_x\hat{\imath} + u_y\hat{\jmath})$$

This concludes the computation of the force field $\boldsymbol{\nu}$.

On the actual modelling side, the starting system was the same as the modelled in the previous section as were the boundary conditions and parameters. To observe the effects caused by imposing the new force field, we monitored regions that had soft phases close to each other, in such a way that bridging them through the hard phase was possible. For the region to be an ideal candidate, three criteria were searched for by visual inspection:

1. Region had soft phases separated by a hard phase by no more than 10 lattice units;
2. The soft phases did not touch or merge for a long number of iterations (i.e. more than 2000);
3. Sufficiently stable evolution, without sudden growth or decay spurs.

Condition 1 arises from the fact that the longer the gap between soft interfaces, the larger the radius of effect of the force. While it is easy to process this modification, a greater radius has a more global effect that would potentially influence unwanted neighbouring phases. In turn, this would muddle the results' clarity. The small limit of 10 lattice units for the gap provided a manageable local force to work with.

The second characteristic is self-evident, as we wanted to see if non-merging soft phases would bridge as consequence of our force field and not the natural evolution of the system.

Finally, the last condition is necessary to account for the phases' normal growth or shrinkage. These swift area changes could be mistaken as being a consequence of our interfering hand. Thus, only regions with stable growth or reduction on time scale of several hundred iterations were acceptable.

For the previous starting conditions, several areas that matched all criteria were quickly found. The starting point for the interface search algorithm was established in the middle of one bridgeable region and the equal simulation parameters used. Several force amplitudes were used to discover the size needed to cause an observable effect and how this effect varies.

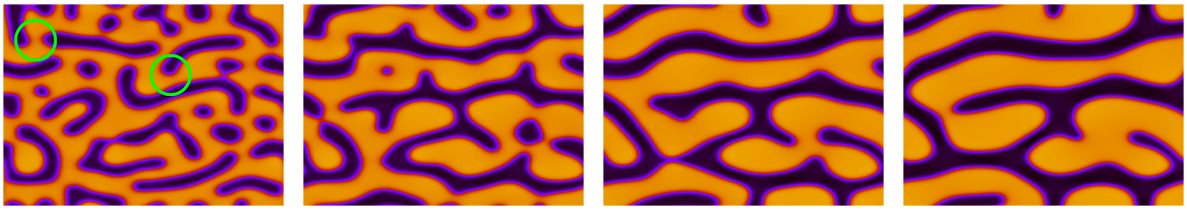

(a) 12100 (b) 22100 (c) 37100 (d) 57100

Figure 2.10: Simulation on a 128 by 128 lattice mesh, with $ge = 0.07$, $\bar{\phi} = 0.2$ and no force field applied ($\boldsymbol{\nu} = 0$). Optimal area for interference (i.e. follows all three criteria) is marked with a green circumference. Iteration number is labelled under each image.

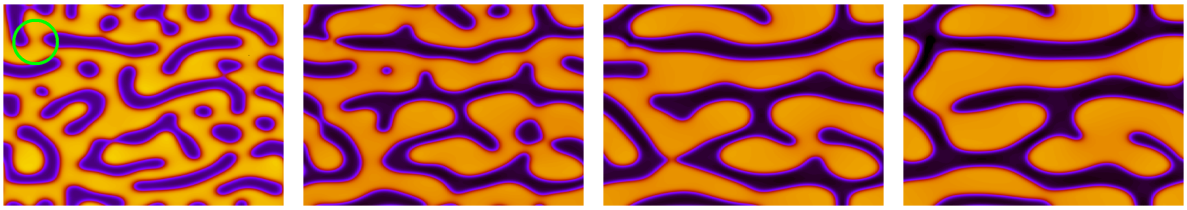

(a) 12100 (b) 22100 (c) 37100 (d) 57100

Figure 2.11: Simulation on a 128 by 128 lattice square mesh, with $ge = 0.07$, $\bar{\phi} = 0.2$, $K = 6$ and force field $\boldsymbol{\nu}$ applied on the green circumference. Iteration number is labelled under each image.

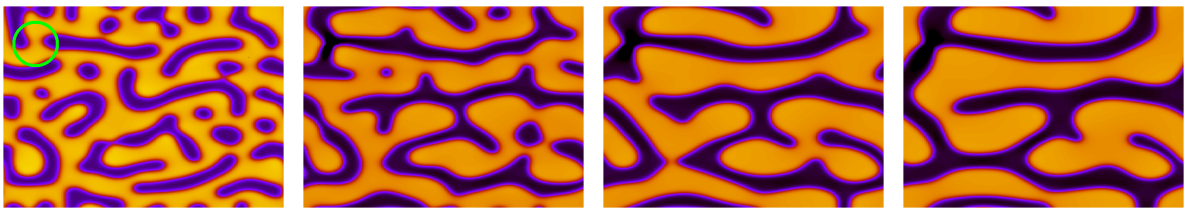

(a) 12100 (b) 22100 (c) 37100 (d) 57100

Figure 2.12: Simulation on a 128 by 128 lattice mesh, with $ge = 0.07$, $\bar{\phi} = 0.2$, $K = 10$ and with force field $\boldsymbol{\nu}$ applied on the green circumference. Iteration number is labelled under each image.

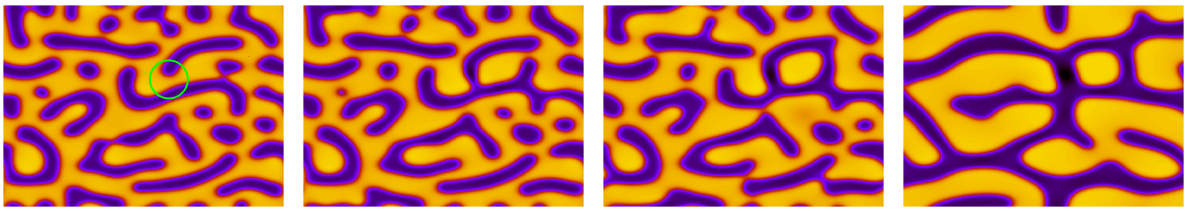

(a) 12100 (b) 14100 (c) 17100 (d) 37500

Figure 2.13: Simulation on a 128 by 128 lattice mesh, with $ge = 0.07$, $\bar{\phi} = 0.2$, $K = 6$ and with force field $\boldsymbol{\nu}$ applied on the green circumference. Iteration number is labelled under each image.

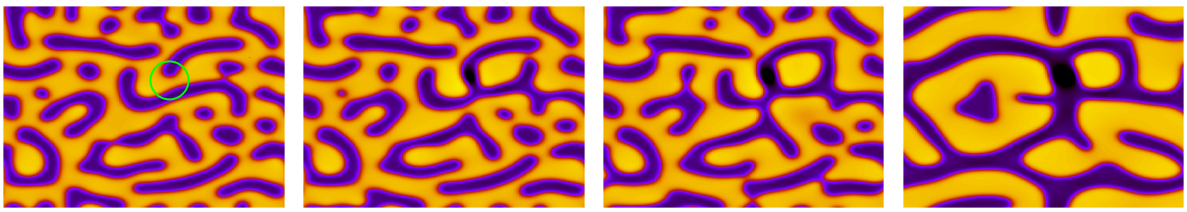

(a) 12100 (b) 14100 (c) 17100 (d) 37500

Figure 2.14: Simulation on a 128 by 128 lattice mesh, with $ge = 0.07$, $\bar{\phi} = 0.2$, $K = 10$ and with force field $\boldsymbol{\nu}$ applied on the green circumference. Iteration number is labelled under each image.

We gathered from the results with different amplitudes that the main difference is the velocity in which the pulling effect or bridging effect occurs. Comparing figure 2.11 and figure 2.12, two simulations where the interference χ was applied in the same location, we see that full bridging takes about 15000 iterations with low amplitude forces ($K = 6$), while with high amplitude forces ($K = 10$) it takes much less than 10000 iterations.

Another consideration is that the amplitude is also responsible for the the thickness of the bridges made, as the interference is applied uninterruptedly. Moreover, because higher amplitudes bridge faster, the changes to the local system structure compared to cases with lower amplitudes are more pronounced, as seen on the images (d) of figures 2.11 and 2.12.

These observations are further confirmed by figures 2.13 and 2.14, where we applied the same interference but in a different location that was also inside the criteria defined above.

In conclusion, the results show that for forces of a certain magnitude the bridging effect is coherent with our expectations. This proof-of-concept was enough to provide a framework that enabled us control over a dual-phase system.

2.4 Blood Vessel without Proliferation

The conclusions gathered from the proof-of-concept model were used to model a more accurate description of an angiogenic system. The initial system was changed to reflect this. An average value with random noise superimposed was discarded in favour of a predominantly hard system with a long, vertical soft phase – our capillary analogue. We also switched the domain's order values, thus, from this point on, the soft-phase will correspond to $\phi = 1$ and the hard-phase to $\phi = -1$.

Evidently, this type of system has no bridgeable soft phases, as there is only one soft phase oriented vertically. Here, we tried to verify if our compressive force field, when applied to the interface, would generate a suitably strong projection of the soft material. If we were indeed capable of forming this protuberance, cell migration could be reasonably emulated.

Firstly, the interference was applied to the interface, at the centre on the right side of the initial capillary as shown in 2.15. The interference direction was, as before, normal to the interface. In this situation, it follows that $\mathbf{u} = (1, 0)$.

In this case, it is easier to see the effect of our influence and the ability of the system to model correctly mechanical stresses. If the vessel's soft material is pulled in the horizontal direction, it is expected that the interface opposite to the one being pulled also responds in a similar manner, due to the mechanical tension of the vessel. Applying χ at the interface causes a increase in the values of ω in two small regions at opposite sides of the interface and a larger decrease in the region around the interfacial point. This is a direct result of the shape of χ as seen in figure 2.8.

Because of the opposing signs of the maps of ω and χ, an increase in ω corresponds to a decrease in ϕ. This way, values of ϕ become more positive near the interface until reaching $\phi = 1$, when they start belonging to the vessel's domain. Also, because of the other two peaks of χ, it is usual to observe a characteristic gray zone inside the capillary, because $\phi < 1$ where it should be $\phi = 1$. Similarly, a black area can be seen outside of it, adjacent to the interface, consequence of $\phi < -1$ instead of the previous $\phi = -1$. This is the reflection of the compressive force field caused in the system. This way, there is a dilation of the vessel caused by the force applied in an area inside it with the direction of the migration, leaving this area with less matter. The other force is applied on the ECM and with its direction towards the interface (opposite to the migration), resulting in a decrease of the value of ϕ in that area, thus compressing it.

It is this mechanism that acts as a mimicry of the mechanical effects we added in the equations. The system responds to these perturbations by filling the less dense spots with surrounding matter to restore the pure valued phases of the system. Hence, the spot that is left with less matter is posteriorly filled by surrounding vessel material, causing the depression in the zone opposite to the interface. The result is a complete simulation of a pulling effect.

Moreover, by applying $\boldsymbol{\nu}$ in a manner similar to a step function we can limit rupture possibility and intensify the reflection of the mechanical tension throughout the capillary's domain. To clarify, the interference is applied during a number of iterations (we called this number of iterations $move$) and then removed. By using this technique, the system is allowed to completely process the strain caused by our influence on the entire vessel. This cool-off period, dubbed $rest$, needs to be longer the larger the strain

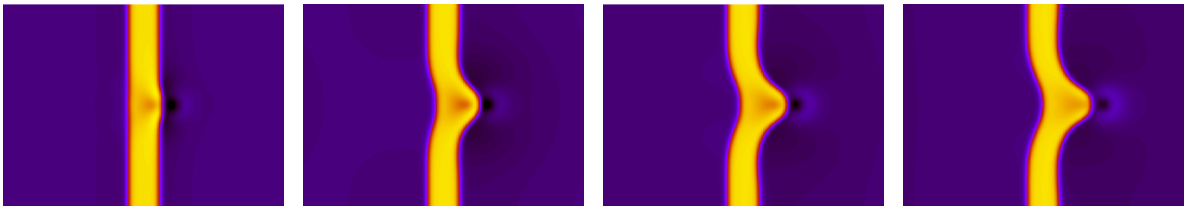

(a) 900 (b) 9000 (c) 18000 (d) 26700

Figure 2.15: Effect of pulling vessel analogue, with $g_E = 0.07$, $K = 20$, duration of interference $move = 2000$ and cool-off period $rest = 300$ on a 128 by 128 lattice mesh. The "black hole" is the consequence of applying χ, as mentioned in the text. A depression is clearly observable in the wall opposite to the interface opposite of the "black hole".

exerted.

The negative effects of not having a cool-off period are displayed in figure 2.16. Here, the area inside the capillary is excessively dilated, causing a grey area inside the vessel's domain that evolves into a rupture (hole in blue on the vessel), which is hard to fill.

With the small addition of a rest period, the system is without interference for some iterations before the force field's centre is recalculated and the force field reapplied. This way, we can see in figure 2.15 that the vessel is dilated (gray area inside the capillary domain), but rupture does not occur. Thus we have the same mechanic characteristics due to the compressive force field as the ones discussed in the previous section (2.3).

(a) 900 (b) 1200 (c) 1500 (d) 1800

Figure 2.16: High amplitude interference without cool-off period to let the system process all the interference's effects resulting in rupture. Simulated with $g_E = 0.07$, $K = 30$ and duration of interference $move = 2000$ on a 128 by 128 lattice mesh.

To bring our model closer to the real case (i.e. the angiogenic process), we had to model chemotaxis, which is indispensable to nourish growth and provide it with directionality. As explained in section 1.3, sprouting angiogenesis follows directional cues of various natures. The most commonly used are chemical cues soluble in the surrounding medium (e.g. VEGF). Thus, permanent sources of these factors are created and allowed to diffuse in the medium. Consequently, two different meshes are modelled. One is the standard order parameter mesh; the other covers the growth factors and their diffusion. To emulate

the diffusible factors, which we termed V, we used the following equation:

$$\frac{\partial V}{\partial t} = D_g \nabla^2 V - \alpha_C \Theta(\phi) V \tag{2.29}$$

$$\text{where } \Theta(\phi) = \begin{cases} 0 & \text{outside the capillary} \\ 1 & \text{inside the capillary} \end{cases}$$

In this equation, $\alpha_C \Theta(\phi) V$ is the consumption term that effectively models the depletion of growth factors by the activated endothelial cells with rate α_C. Also, D_g is the diffusion constant of the growth factors.

In this simulation, several sources of factors are added at predefined locations; normally they were arranged in tight clusters, so that it was easier to verify if the sprout followed the chemical signals correctly. As with the biological case, these sources continue releasing factors until they are in close proximity to an endothelial mesh. That reaction was mimicked in the model by shutting off the sources when they were at a small radial distance to the interface.

With the addition of V, the direction of cell migration would no longer be normal to the interface, but in the direction on the greatest concentration of chemotactic factors. For this reason, the interface-finding algorithm had to be changed. Now, because the direction of the gradient at the tip cell could change abruptly, the algorithm stored each gradient in order to find the tip cell's position after the change to the vessel. Thus, after finding the first interface point and applying the interference, this new algorithm proceeds in the following order:

1. Move the point in the gradient's direction a length equal to the maximum diameter of the gaussian used to formulate ν;
2. Move backwards in this same direction until an interface is reached;
3. Calculate the new gradient at this point, apply $\boldsymbol{\nu}$ and repeat from '1.'.

The time evolution algorithm was then changed to include this new mesh. It calculates an interfacial point I and then the gradient of the chemotactic factors calculated, which corresponds to calculating the point gradient of the V mesh:

$$\begin{aligned} \nabla V_I &= \nabla_x V_I \, \hat{\imath} + \nabla_y V_I \, \hat{\jmath} \\ &= \frac{\partial V_{x_I, y_I}}{\partial x} \hat{\imath} + \frac{\partial V_{x_I, y_I}}{\partial y} \hat{\jmath} \\ &= \nabla_x V_{x_I, y_I} \, \hat{\imath} + \nabla_y V_{x_I, y_I} \, \hat{\jmath} \end{aligned}$$

approximating with finite differences:

$$\nabla V_I \simeq \frac{V_{x_I+1, y_I} - V_{x_I-1, y_I}}{2} \, \hat{\imath} + \frac{V_{x_I, y_I+1} - V_{x_I, y_I-1}}{2} \, \hat{\jmath} \tag{2.30}$$

The algorithm's next step is to calculate the interference with the direction of the gradient and then apply it intermittently. As before, no new material is introduced to the order mesh, hence it is expected that the vessel analogue be only pulled towards the greatest concentration of growth factors.

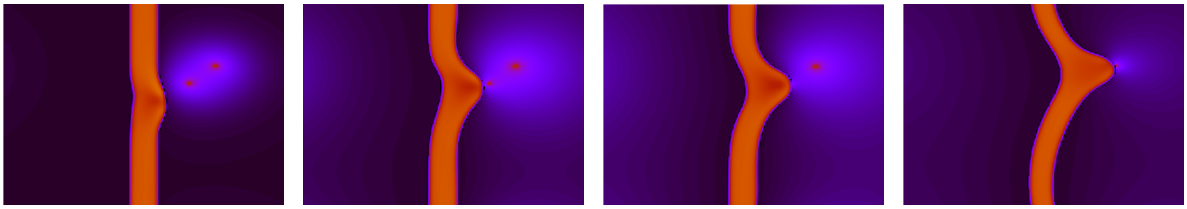

(a) 3000 (b) 16800 (c) 28200 (d) 149100

Figure 2.17: Migration towards sources of V (greatest concentration of V) without proliferation, due to χ, with $K = 20$, $g_E = 0.07$, $\alpha_C = 0.15$ and $D_g = 0.6$. Notice that the capillary analogue is actually pulled and not just stretched.

Our results for this phase show that implementing directional migration was accomplished. As shown in figure 2.17, the vessel is continuously dilated and the ECM mesh in front of it compressed, emulating endothelial cell migration. In this figure, the vessel first travels towards the highest available concentration of growth factors (the leftmost source). Upon reaching this source, the vessel further travels towards the last source. Notice that at each step the capillary behaves as if it is being pulled and its migration is completely directional, which was our goal in this section.

A consequence of the shape of our force field ν, specially its related interference χ, is that when the tip cell senses a very abrupt gradient direction (i.e. tangent to the interface) it migrates very fast in a thin, spike-like fashion as can be observed in figure 2.18. Observing how we apply χ to the interface, we can see that in this situation the peaks that decrease ϕ, which normally cause the gray area inside the vessel and black area in the ECM, are both outside the vessel, while the ϕ increasing peak lies centred at the interface. This causes our interference to dilate the vessel very quickly and thinly in the direction perpendicular to the perceived gradient. In the figure mentioned, due to the source close to the vessel, the gradient calculated at the tip cell has a predominantly vertical heading. Thus, χ will be applied in a way that its ϕ increasing peak is wider in the horizontal direction, causing quick extension of the vessel in that direction.

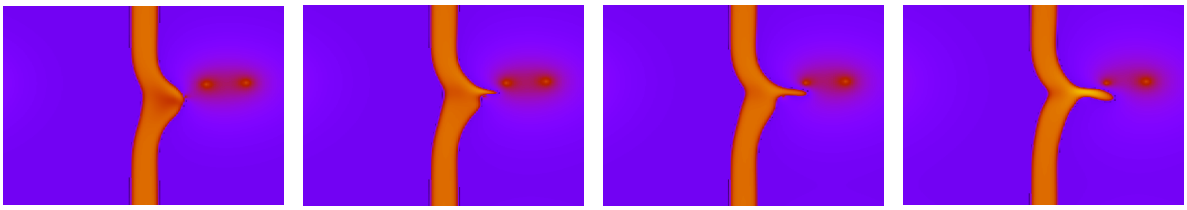

(a) 10800 (b) 12600 (c) 13800 (d) 17400

Figure 2.18: Simulation of migration of a vessel without proliferation with $g_E = 0.07$, $D_g = 0.3$ and $\alpha_C = 0.65$ on a 128 by 128 lattice mesh with iteration number below each image.

2.5 Blood Vessel with Proliferation

As seen in the previous section, we were capable of pulling and stretching a capillary vessel. However, angiogenesis also has a proliferative portion. From the literature, we gathered that both the mechanical stimulus[18] and the growth factor concentration can increase endothelial cell proliferation[31]. Thus, any new material added to the system would have to be proportional to these factors.

Here, we use a soft-phase vessel analogue, hence, an increase in matter would translate in an increase of the ratio of soft-phase to hard-phase in the system. As usual, we track the average order value; if more matter is added, this value would increase.

For this effect, we altered the main equation responsible for the phase dynamics, equation (2.25) to:

$$\begin{aligned}\frac{\partial\phi}{\partial t} = \nabla^2\left[\phi^3 - \phi - \nabla^2\phi + g_E\,\hat{Q}\right] + 2g_E\sum_{i,j}\partial_{ij}\left\{\phi\left[\partial_{ij}\,\omega - \frac{1}{d}\,\delta_{ij}\nabla^2\omega\right]\right\} \\ + (1-\phi)\Theta(1-\phi)\left(\kappa_{\boldsymbol{\nu}}\chi\Theta(\chi) + \Theta(\phi)\kappa_V V\right)\end{aligned} \tag{2.31}$$

where κ_V is the proliferation constant due to applied force, $\kappa_{\boldsymbol{\nu}}$ is the proliferation constant due to the concentration of V, $\Theta(\phi)$ is the same as the one in (2.29), $\Theta(1-\phi)$ is easily deduced from the same equation, and $\Theta(\chi)$ is the Heaviside step function, which nullifies the respective term for negative values of χ.

Several considerations from the above equation must be discussed. First, notice that (2.31) differs from (2.25) by $(1-\phi)\Theta(1-\phi)\left(\kappa_{\boldsymbol{\nu}}\chi\Theta(\chi) + \Theta(\phi)\kappa_V V\right)$. Individually, they represent the proliferation rates of the two distinct signals above described.

The first term, $(1-\phi)\Theta(1-\phi)\kappa_{\boldsymbol{\nu}}\chi\Theta(\chi)$, is proportional to the result of the force field $\boldsymbol{\nu}$. Thus, this proliferation should be proportional to the trace of the deformation tensor. In our case, using (2.18) and (2.21) and (2.28), we know that $\nabla.\mathbf{u} = \nabla^2\omega = \phi - \bar{\phi} + K\chi$, from where we can conclude that this proliferation becomes higher with increasing χ. Because of this fact, we write our term as proportional to χ.

This type of proliferation can only occur when tension is applied (i.e. $\chi \neq 0$). In order to mimic cell division, we want to add new matter to areas adjacent to where vessel matter already exists, hence the term proliferation. Due to the nature of the pulling effect, by being proportional to χ, which is applied near the interface and influences the surrounding vessel and ECM, this proliferation occurs in the desired area.

As we do not want to have new material being added inside the vessel, where $\phi = 1$, we use $(1-\phi)$. This factor also causes the system to be better behaved and reduces the probability of fluctuations inside the pure domain (i.e. $\phi > 1$ instead of $\phi = 1$) because it dampens the proliferative effect for increasing ϕ. The other factor, $\Theta(1-\phi)$, allows us to dismiss the cell division effect for local values of $\phi > 1$ that occur due to small fluctuations inside each pure domain. This way, we prevent proliferation inside the vessel's domain that occurs due to the radius of χ affecting an area that encompasses not just the interface but parts of the ECM and capillary and lessen some possibly disruptive effects.

An important concept here, is that $\boldsymbol{\nu}$ is conservative, as such, χ is also conservative. Because our goal is to add proliferation, which increases the amount of matter in the system, we only want to use the

positive values of χ. This way, this proliferative term is still proportional to the tension applied on the interface, however it is only proportional to its positive part - thus the use of $\Theta(\chi)$.

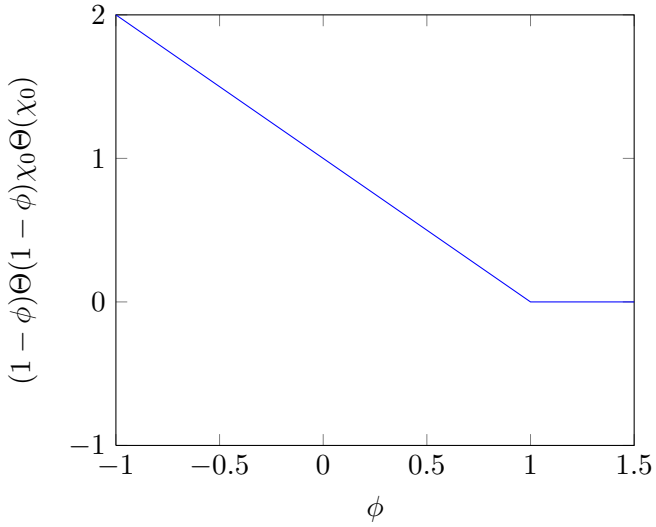

Figure 2.19: Value of the proliferative term proportional to χ varying with ϕ. In this plot $\kappa_\nu = 0.05$ and the value of χ was made constant $\chi_{constant} = \chi_0 = 20$. Notice that when inside the capillary analogue ($\phi = 1$ or $\phi > 1$) this term has no influence.

The second term is proportional to the concentration of growth cues surrounding the vessel. Thus, the new matter that this term brings is simply proportional to the value of the concentration of factors. However, like for the other term, we only want proliferation adjacent to the vessel. Consequently, we used $\Theta(\phi)$, $(1-\phi)$ and $\Theta(1-\phi)$ so that there would only be proliferation near the vessel (i.e. in the interface: $0 < \phi < 1$).

Cases with only one type of proliferation and both types simultaneously were run. We noticed that cell multiplication due to the concentration of growth factors resulted in a bloating effect of the entire capillary. We can see in figure 2.20 that the vessel gets thicker the longer the simulation is run. Even by using a lower constant, the vessel's diameter is bloated, albeit slightly.

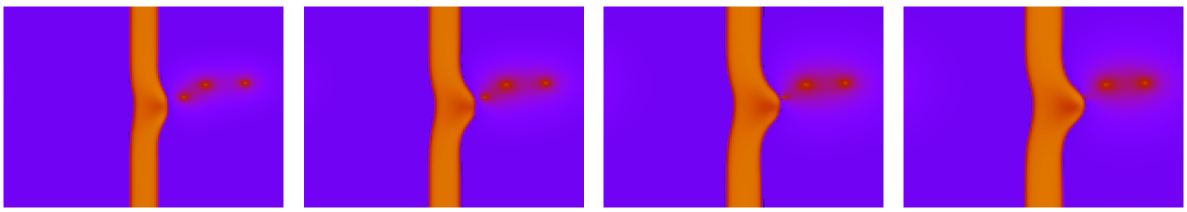

(a) 3000 (b) 5400 (c) 8400 (d) 11800

Figure 2.20: Simulation on a 128 by 128 lattice mesh of migration of a vessel with proliferation proportional to the concentration of growth factors, with $g_E = 0.07$, $D_g = 0.9$, $\alpha_C = 0.1$, $\kappa_V = 0.3$.

In the tension proportional case, a bloating effect could also be observed, however much smaller and mostly in the migration's direction. By using this type of proliferation, we got results that better

emulated proliferation during migration. In figure 2.21 we can observe that the proliferation results from the material bound to migrate forward. As mentioned in 1.3, proliferation during migration happens mostly at the stalk of the sprout. Thus, our proliferative term proportional to the tension is in accordance to the literature.

Combining the two terms, our simulations returned the images plotted in figure 2.22. We used a larger value of $\kappa_{\boldsymbol{\nu}}$ and smaller value of κ_V because the proliferation with the direction of migration is more controlled and returns more coherent results as mentioned above. In this figure we can see the migration towards the sources of factors on the right and that the vessel analogue is not just pulled, but has new material at every step during the movement. Also, the influence of proliferation proportional to V can still be observed from the dilation of the vessel's diameter. Notice that the vessel still reacts mechanically to the tensions imposed, as can be seen from the slight curve at the interface opposite of the migration. However, the dilation effect from the pulling force is focused on the new material, serving as a buffer of sorts, thus diminishing the curvature effect so prevalent in the simulations without proliferation.

These simulations proved that proliferation proportional to χ is a more realistic approach to the cell division that occurs during cell migration.

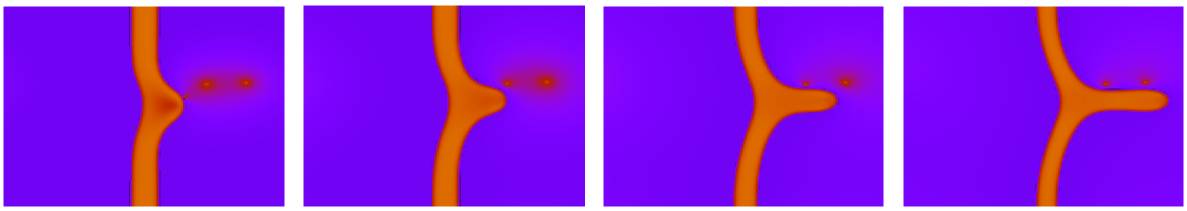

(a) 2400 (b) 11100 (c) 22200 (d) 33300

Figure 2.21: Simulation of migration of a vessel with proliferation proportional to the interference χ, with $g_E = 0.07$, $D_g = 0.5$, $\alpha_C = 0.25$, $\kappa_{\boldsymbol{\nu}} = 0.03$ on a 128 by 128 lattice mesh. Notice that the migration is mostly perpendicular to the main vessel after encountering the first source of factors, which is discussed in the next chapter.

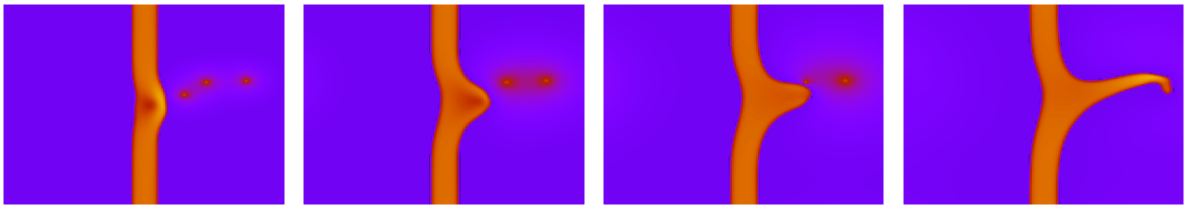

(a) 2400 (b) 11100 (c) 22200 (d) 33300

Figure 2.22: Simulation of migration of a vessel with proliferation proportional to the tension and concentration of growth factors, with $g_E = 0.07$, $D_g = 0.2$, $\alpha_C = 0.85$, $\kappa_{\boldsymbol{\nu}} = 0.001$ $\kappa_{\boldsymbol{\nu}} = 0.001$ and $\kappa_V = 0.002$ on a 128 by 128 lattice mesh.

2.6 Final Model

The cellular environment is highly dynamic with various processes of the same kind happening in quick succession or simultaneously. It stands to reason that our next step was to include an increasing the number of initial stimuli. Therefore, we adapted our routines to follow several concurrent movements.

The change to the model is minimal: the interface-finding algorithm remains the same, but is applied sequentially to each migration routine. This way we track a number of points equal to the number of different areas where pulling events occur.

We used both types of proliferation simultaneously, with prevalence of cell division proportional to tension over proliferation proportional to concentration of growth factors, as the vessel bloating effect it causes was undesired.

As this is the final section of the model development, we will present the results and their discussion in the next chapter.

As a summary of the parameters used to control the system, we have the following table:

Parameter	*Description*	*Most used values*
h	Stepping value for finite difference approximations	1
size	Number of lattice of the square mesh used for simulations	128
Δt	Step size used in the simulation	0.02
K	Amplitude of the applied interference χ	20
g_E	Influence of the equation's elastic terms.	0.07
$\bar{\phi}_0$	Initial value of the average order parameter.	0.2
D_g	Diffusion of growth factors	0.7
D	Diffusion of the order parameter	1
α_C	Consumption rate of growth factors.	0.25
r	Radius of applied interference χ	4
$move$	Duration of application of χ (duration of each migration sequence)	2000
$rest$	Cool-off period after applying interference	300

Table 2.1: List of parameters used in the various simulation and their optimal values, relative to the last model.

Exploring the Model

3.1 Final Results and Parameter Discussion

The results obtained from the model in section 2.6 are indicative of the capability of our model to accurately simulate multiple pulling events in different areas with and without proliferation.

By gathering information from the previous simulations we could better adapt the parameters used to our purposes. We noticed that a low value for the diffusion of growth factors D_g caused a slow initial migration, due to the non-existence of factors near the vessel's interface to guide migration. However, a high value would cause a saturated area very quickly in the vicinity of the sources and increase the probability of abrupt or erratic migration directions.

Another important concept is the effect of the consumption constant α_C. It controls the rate of depletion of growth factors inside the vessel's domain and interface. By using a high value of α_C we effectively remove growth factors in these areas, in turn, when a migration event occurs and we calculate the gradient at the tip cell (a point in the interface) it will be almost perpendicular to the interface instead of correctly pointing in the direction of growing concentration. This occurs because there is no concentration of growth factors in the capillary's domain, while there is some non-zero concentration value on the extracellular medium, which causes the computation of the gradient (see (2.30)) to have a very high value in the direction perpendicular to the interface compared to the value in the tangent direction. With a low value of consumption rate, the value of V inside the vessel is scaled down, instead of being null, dismissing the predominance of the gradient's term in the perpendicular direction on the overall migration direction. This way, the gradient will correctly assess the concentration V.

The effect of a high consumption rate α_C can be observed in some results of section 2.5, specifically figure 2.22, which used $\alpha_C = 0.85$. We can see that the vessel extension having curved initially to intersect the first source of V then moves relatively perpendicular to the main vessel. Thus, using a low value of α_C we can mimic the effect of consumption of growth factors by the vessel while decreasing the probability of forced migration direction.

For the results without proliferation, we see an added stress on the capillary when two migrations occur. This stems from the two forces pulling part of the vessel in different directions. These effects are illustrated in figure 3.1 and they represent an interesting case to observe, as it further demonstrates the effect of the mechanical features incorporated. In this figure, we see a vessel being continuously pulled in two opposite directions as the tip cell migrate towards the sources in the lower left and upper right. Notice that the thickness of the central area of the vessel is stretched and, by the end, is much thinner than

initially.

In the case where proliferation was added (figure 3.2), we see an initial migration of the tip cells towards the cluster of sources. When they overtake the upper sources at each respective corner, they begin looping towards the bottom as a consequence of the factors still being diffused by the lower sources.

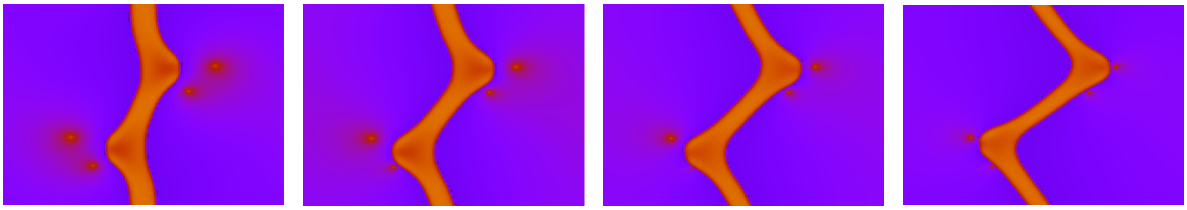

(a) 15000 (b) 45000 (c) 65000 (d) 120000

Figure 3.1: Two simultaneous migrations without proliferation. Using $g_e = 0.07$, $K = 20$, $D = 0.6$ and $\alpha_C = 0.15$ for the simulation on a 128 by 128 lattice mesh.

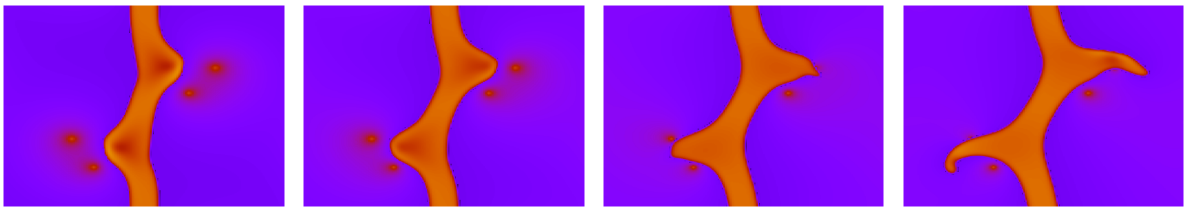

(a) 9000 (b) 15600 (c) 25200 (d) 32400

Figure 3.2: Two simultaneous migrations with cell division. Using $g_e = 0.07$, $K = 20$, $D = 0.5$, $\kappa_{\boldsymbol{\nu}} = 0.001$, $\kappa_{\boldsymbol{\nu}} = 0.0001$ and $\alpha_C = 0.7$ for the simulation on a 128 by 128 lattice mesh.

3.2 Vessel Regression

Astonishingly, in some simulations vessel regression was observed. According to literature [13], this usually occurs during tip cell competition, when migration is led in a direction that does not provide sufficient stimulus. Here, we observed this phenomenon multiple times. In some cases it occurred during an overtake of a source of factors, causing its next potential migration direction to be highly erratic and, thus, in the wrong direction. However, the majority of occurrences was caused by the limited probing scope of the single tip cell that led it in a direction with a scarce concentration of factors. Usually, this happens when there is still a significant concentration of factors diluted in the medium. The result is a vessel that is retracted, with a possible new extension in a better direction (i.e. greater concentration of V). This is the case in simulation 3.3, where we can clearly see regression of a vessel in favour of extension in another direction.

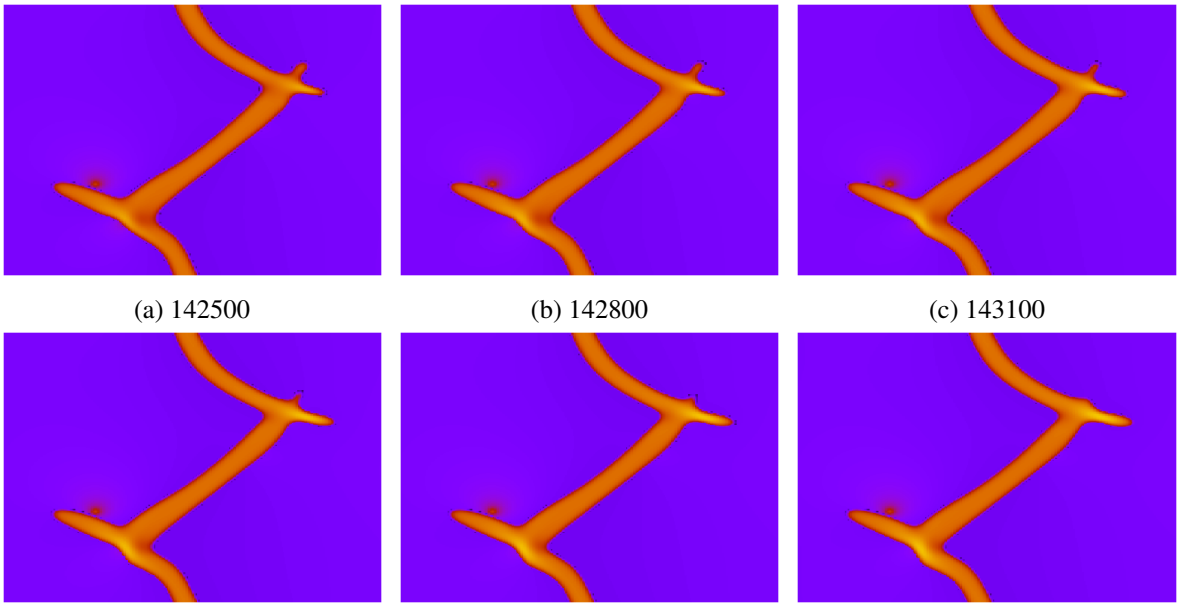

(a) 142500 (b) 142800 (c) 143100

(d) 143400 (e) 143700 (f) 144000

Figure 3.3: Capillary vessel regression in a non-proliferative system observed in the right side. After having migrated in a direction that did not provide enough factors for continued migration, the vessel protrusion retracts. Using $g_e = 0.07$, $K = 20$, $D = 0.9$, and $\alpha_C = 0.2$ for the simulation on a 128 by 128 lattice mesh.

In figure 3.4 we notice that the main vessel extension travels just below the two sources of growth factors. One of the side protrusions extends and migrates in the opposite direction of the sources, consuming some factors diffused in the medium. As their availability runs out, the vessel is retracted.

Another example of regression on a long migration is observable in figure 3.5. In this simulation, after having consumed and shut off the closest sources, the sprout migrates towards the last source. Upon reaching it, due to the gradient's verticality, a spike like projection is emitted. As migration continues forward, in order to consume the remaining growth factors still in the environment, the lower extension

retracts into the main branch.

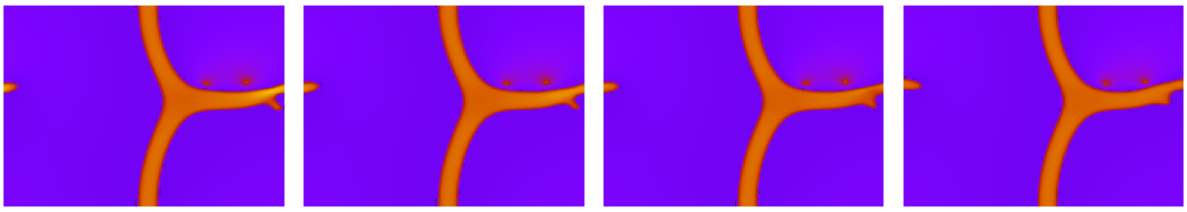

(a) 76200 (b) 76800 (c) 77100 (d) 78200

Figure 3.4: Capillary vessel regression on a system with proliferation. After having consumed the leftover factors diffused below the main vessel, this protrusion retracts. Using $g_e = 0.07$, $K = 20$, $D = 0.4$, $\kappa_{\boldsymbol{\nu}} = 0.0005$, and $\alpha_C = 0.4$ for the simulation on a 128 by 128 lattice mesh.

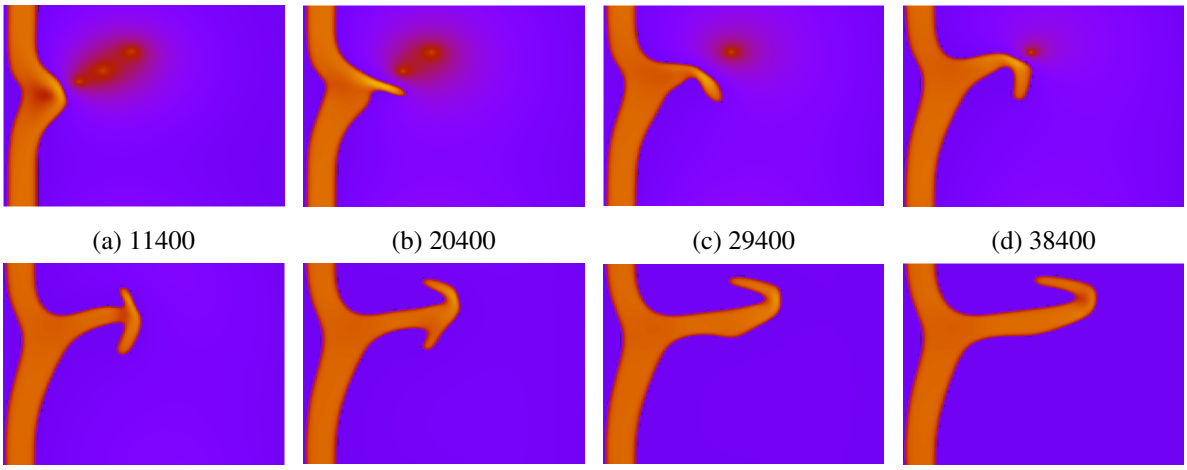

(a) 11400 (b) 20400 (c) 29400 (d) 38400

(e) 47400 (f) 56400 (g) 64400 (h) 73400

Figure 3.5: Capillary vessel regression on a system with proliferation. The vessel retracts after migration towards the last source occurs. Using $g_e = 0.07$, $K = 20$, $D = 0.7$, $\kappa_{\boldsymbol{\nu}} = 0.01$, and $\alpha_C = 0.25$ for the simulation on a 128 by 128 lattice mesh.

3.3 Simulation Speed

Another consideration we took during all the modelling process was simulation speed. Obviously, having results faster is always useful, especially for debugging and task-farming parameters. We used the compiler's most aggressive optimization flags which can sometimes alter the behaviour of some parts of the code and, therefore, the results. We proceeded with using this type of optimization after checking that its effect on the code and results was neutral.

Also, shared memory parallelisation was used by the means of openMP. This parallelised code was run on a desktop computer with a *Intel core i7 960 2.66 GHz* (4 cores - 8 threads) processor with the maximum available threads.

Combining both the compiler's own optimizations and the type of parallelization mentioned we got speed increases of over 1700% compared to the unoptimised version.

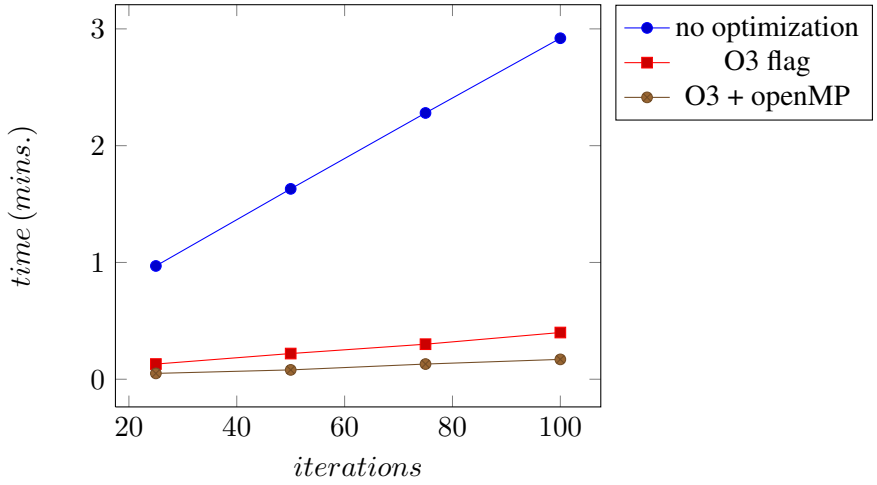

Figure 3.6: Comparison between code efficiency for the same script (the one used in section 2.4) obtained through external optimization.

Changing our method of solving linear equations was also tried to increase efficiency. We started by using a simple Gauss-Jacobi method. We then used Gauss-Seidel and Successive Over Relaxation (SOR). Our main focus would be to use these methods in the computation of ω and χ. However, calculating χ is not a cumbersome task, as it is only necessary when an interference needs to be calculated. This is not the case with ω, which is computed at every iteration and needs to be very accurate.

Replacing the Jacobi method by the Gauss-Seidel method resulted in an increase in speed of convergence for the same accuracy for the non-optimised case. Nevertheless, with compiler optimization turned on, we saw a decrease compared to the same optimization using a Jacobi method, forcing us to discard this method.

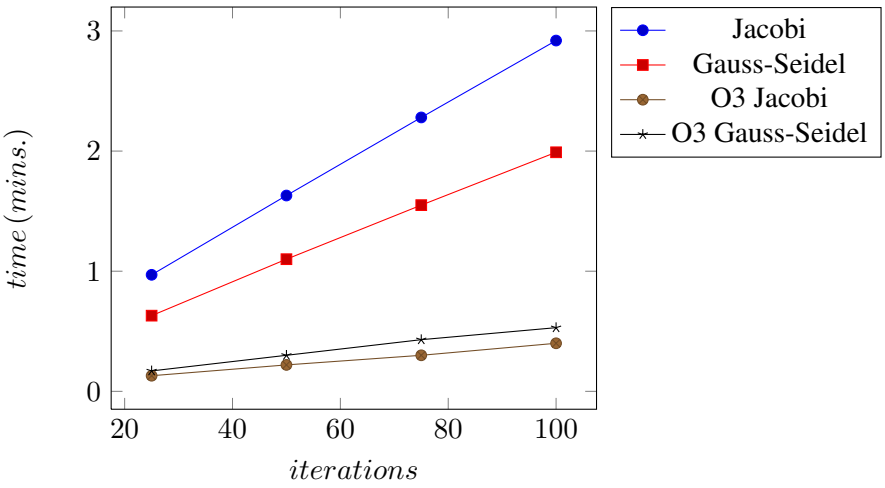

Figure 3.7: Comparison between code efficiency for the same script obtained through internal optimization.

Conclusion and Future Work

Our steps during the Model Development chapter clearly demonstrate the success of including mechanical traits on a continuum based phase-field model. We obtained a full simulation of a vessel that could be pulled in several directions and acted accordingly to our expectations. The inclusion of the proliferation was also a success and can be manipulated in different ways, in order to correspond to the real cell environment.

In its current state, it serves as a good basis for further development that include the standard routines that are already used in the community. Some of those examples include branching of vessels and automatic initiation of angiogenesis depending on a certain stimulus, commonly concentration of growth factors [30].

Another possible step is to include real mechanotactic cues that stimulate the growth when a determined mechanical attachment is made (e.g. binding to the source of growth factors). We can not overlook that this step increases the accuracy of the model, as in the real case we have a heterogeneous ECM. Its importance is still a matter of study in both the biologic perspective and the computational perspective.

Our addition of the elastic energy on the Ginzburg-Landau free-energy functional exemplifies how additional manipulations can be made to include other important effects in a biological systems, e.g. penalize changing the tissue's curvature, to help control topology alterations.

Several minor improvements to the tip cell analogue can also be made. Its scope could be increased and less prone to lead in erroneous migration direction by, for example, averaging gradient direction at several points instead of just one.

Creating a full three dimensional model from our work is a possibility. Most of the equations can describe the effects of a three dimensional environment by changing the dimension parameter d. The remaining work would be to adapt the search algorithm and reformulate or recreate the shape of the interference to work in three dimensions.

As our goal did not include parametrisation of this work we can provide a more concrete biological foothold for the model by studying *in vitro* the real values for some of constants used.

The additional objective of creating a full parallelised code that would run on a shared memory system was only partially fulfilled. Thus it remains as work for a posterior occasion.

With more development, this type of implementation could further our understanding of the complex mechanic influences present in the dynamic cell environment and provide an interesting and more informative analogy of the real case.

Ostwald Ripening discussion

Ostwald Ripening is a spontaneous occurring process, which, in our case, corresponds to a decrease in size of small domains and subsequent increase of the size of large domains. The explanation to this phenomenon lies in the fact that ,*thermodynamically*, large domains are favoured over small domains. This is a consequence of particles in the surface being energetically less stable as their are bound to less neighbours than those in the interior. So, because of interfacial energy considerations, smaller domains are less stable than their larger counterparts.

An important aspect of this phenomenon can be better described by the Kelvin equation if we dismiss nucleation events. This equation, at constant temperature T, can be expressed as:

$$\ln \frac{p}{p_0} = \frac{2\gamma V_m}{rRT}$$

where p is the vapour pressure, p_0 is the saturated vapour pressure (which is constant for constant temperature), γ is the surface tension and V_m is the molar volume, r is radius of the domain and R is the universal gas constant.

From this equation we can deduce that, for some fluid, by maintaining γ and V_m, approximately fixed and decreasing r, the vapour pressure p increases. Particles detach themselves from the surface of the domain and dilute in the medium when $p > p_0$, thus domains smaller than a certain value of r will progressively decrease until being completely diluted, causing a saturated environment. When $p < p_0$, which occurs in large domains, the saturated free molecules tend to condense on the surface of the large domains, increasing their size[27].

In conclusion, the smaller domains continuously decrease in size and fuel the growth of large domains in order to minimise the system's overall energy as depicted in figure A.1.

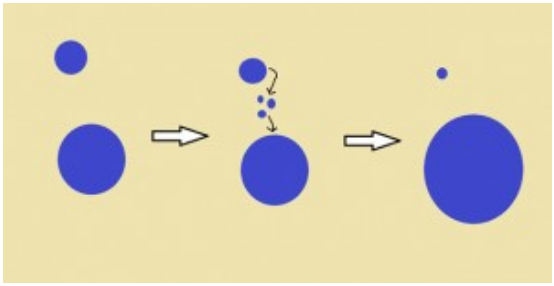

Figure A.1: Domain dynamics during *Ostwald Ripening* phenomenon.

Deduction of elastic energies

The first and zeroth order elastic energies used in section 2.2 are calculated below.

For the zeroth-order:

$$\begin{aligned}
f_{el}^0 &= \frac{\alpha^2}{2L_0^2}K(\nabla^2\omega)^2 + \frac{\mu_0\alpha^2}{4L_0^2}\left(\partial_{ij}\omega + \partial_{ij}\omega - \frac{2}{d}\delta_{ij}\nabla^2\omega\right)^2 \\
&= \frac{\alpha^2}{2L_0^2}K(\nabla^2\omega)^2 + \frac{\mu_0\alpha^2}{L_0^2}\left(\partial_{ij}\omega - \frac{1}{d}\delta_{ij}\nabla^2\omega\right)^2 \\
&= \frac{\alpha^2}{2L_0^2}K(\nabla^2\omega)^2 + \frac{\mu_0\alpha^2}{L_0^2}\left(\partial_{ij}\omega\partial_{ij}\omega + \frac{1}{d^2}\delta_{ij}\delta_{ij}(\nabla^2\omega)^2 - \frac{2}{d}\partial_{ij}\omega\delta_{ij}\nabla^2\omega\right) \\
&= \frac{\alpha^2}{2L_0^2}K(\nabla^2\omega)^2 + \frac{\mu_0\alpha^2}{L_0^2}\left(\partial_{ij}\omega\partial_{ij}\omega + \frac{1}{d}(\nabla^2\omega)^2 - \frac{2}{d}(\nabla^2\omega)^2\right) \\
&= \frac{\alpha^2}{2L_0^2}\phi^2\left(K - \frac{2\mu_0}{d}\right) + \frac{\mu_0\alpha^2}{L_0^2}\partial_{ij}\omega\partial_{ij}\omega \\
&= \frac{\alpha^2(L_0 - 2\mu_0)}{2L_0^2}\phi^2 + \frac{\mu_0\alpha^2}{L_0^2}\partial_{ij}\omega\partial_{ij}\omega \\
&= \frac{\alpha^2}{2L_0}\phi^2 - \frac{\alpha^2\mu_0}{L_0^2}\phi^2 + \frac{\alpha^2\mu_0}{L_0^2}\partial_{ij}\omega\partial_{ij}\omega
\end{aligned}$$

For the first-order some pre-calculations are necessary, because of combinations of shear strain tensors e_{ij}^0 and e_{ij}^1 below:

$$f_{el}^1 = K\nabla.\mathbf{u}^0\nabla.\mathbf{u}^1 + \frac{\mu_1}{4}\phi e_{ij}^0 e_{ij}^0 + \frac{2\mu_0}{4}e_{ij}^1 e_{ij}^0 \tag{B.1}$$

Thus, we compute each order of the strain tensors and then their multiplicative terms. Individually, the strains have the following formulation:

$$\begin{aligned}
e_{ij}^0 &= -\frac{2\alpha}{L_0}\left(\partial_{ij}\omega - \frac{\alpha}{dL_0}\delta_{ij}\phi\right) \\
&= -\frac{2\alpha}{L_0}\left(\partial_{ij}\omega - \frac{1}{d}\delta_{ij}\nabla^2\omega\right) \\
e_{ij}^1 &= \left(\partial_j u_i^1 + \partial_i u_j^1 - \frac{2}{d}\delta_{ij}\nabla.\mathbf{u}^1\right)
\end{aligned}$$

Combining them:

$$
\begin{aligned}
e^0_{ij}e^0_{ij} &= \frac{4\alpha^2}{L_0^2}\left(\partial_{ij}\omega - \frac{1}{d}\delta_{ij}\nabla^2\omega\right)\left(\partial_{ij}\omega - \frac{1}{d}\delta_{ij}\nabla^2\omega\right) \\
&= \frac{4\alpha^2}{L_0^2}\left(\partial_{ij}\omega\partial_{ij}\omega - \frac{2}{d}(\nabla^2\omega)^2 + \frac{1}{d}(\nabla^2\omega)^2\right) \\
&= \frac{4\alpha^2}{L_0^2}\left(\partial_{ij}\omega\partial_{ij}\omega - \frac{1}{d}(\nabla^2\omega)^2\right) \qquad \text{(B.2)}
\end{aligned}
$$

and:

$$
\begin{aligned}
e^0_{ij}e^1_{ij} &= -\frac{2\alpha}{L_0}\left(\partial_{ij}\omega - \frac{1}{d}\delta_{ij}\nabla^2\omega\right)\left(\partial_j u_i + \partial_i u^1_j - \frac{2}{d}\delta_{ij}(\nabla.\mathbf{u}^1)\right) \\
&= -\frac{2\alpha}{L_0}\left(\partial_{ij}\omega\partial_j u^1_i + \partial_{ij}\omega\partial_i u^1_j - \frac{2}{d}\nabla^2\omega\nabla.\mathbf{u}^1 - \frac{2}{d}\nabla^2\omega\nabla.\mathbf{u}^1 + \frac{2}{d}\nabla^2\omega\nabla.\mathbf{u}^1\right) \\
&= -\frac{4\alpha}{L_0}\left(\partial_{ij}\omega\partial_j u^1_i - \frac{1}{d}\nabla^2\omega\nabla.\mathbf{u}^1\right) \qquad \text{(B.3)}
\end{aligned}
$$

Finally, we have the first order elastic energy by replacing (B.3) and (B.2) in (B.1):

$$
f^1_{el} = -\frac{K\alpha}{L_0}\nabla^2\omega\nabla.\mathbf{u}^1 + \frac{\mu_1\alpha^2}{L_0^2}\phi\left(\partial_{ij}\omega\partial_{ij}\omega - \frac{1}{d}(\nabla^2\omega)^2\right) - \frac{2\mu_0\alpha}{L_0}\left(\partial_{ij}\omega\partial_j u^1_i - \frac{1}{d}\nabla^2\omega\nabla.\mathbf{u}^1\right)
$$

Bibliography

[1] B. Alberts, D. Bray, K. Hopin, A. Johnson, J. Lewis, M. Raff, K. Roberts, and WalterP. *Essential cell biology*. Garland Science, New York and London, 2004. ISBN 0-8153-3481-8. 1.3.4

[2] Bruce Alberts, Alexander Johnson, Julian Lewis, Martin Raff, Keith Roberts, and Peter Walter. *Molecular Biology of the Cell, Fourth Edition*. Garland Science, 2002. ISBN 0815332181. URL http://www.amazon.com/Molecular-Biology-Cell-Fourth-Edition/dp/0815332181. 1.3.1

[3] R P Araujo and D L S McElwain. A history of the study of solid tumour growth: the contribution of mathematical modelling. *Bulletin of mathematical biology*, 66(5):1039–91, September 2004. ISSN 0092-8240. doi: 10.1016/j.bulm.2003.11.002. URL http://www.ncbi.nlm.nih.gov/pubmed/15294418. 1.1

[4] A.J. Bray. Theory of phase-ordering kinetics. *Advances in Physics*, 43(3):357–459, June 1994. ISSN 0001-8732. doi: 10.1080/00018739400101505. URL http://dx.doi.org/10.1080/00018739400101505. 2.1

[5] Peter H Burri, Ruslan Hlushchuk, and Valentin Djonov. Intussusceptive angiogenesis: its emergence, its characteristics, and its significance. *Developmental dynamics : an official publication of the American Association of Anatomists*, 231(3):474–88, November 2004. ISSN 1058-8388. doi: 10.1002/dvdy.20184. URL http://www.ncbi.nlm.nih.gov/pubmed/15376313. 1.4, 1.4.1, 1.4.2

[6] A. R. Denton and N. W. Ashcroft. Vegard's law. *Phys. Rev. A*, 43:3161–3164, Mar 1991. doi: 10.1103/PhysRevA.43.3161. URL http://link.aps.org/doi/10.1103/PhysRevA.43.3161. 2.2

[7] Charles A Easley, Claire M Brown, Alan F Horwitz, and Robert M Tombes. CaMK-II promotes focal adhesion turnover and cell motility by inducing tyrosine dephosphorylation of FAK and paxillin. *Cell motility and the cytoskeleton*, 65(8):662–74, August 2008. ISSN 1097-0169. doi: 10.1002/cm.20294. URL http://www.pubmedcentral.nih.gov/articlerender.fcgi?artid=2830206&tool=pmcentrez&rendertype=abstract. 1.3.6

[8] William D. Figg and Judah Folkman. *Angiogenesis: An Integrative Approach from Science to*

Medicine (Google eBook). Springer, 2008. ISBN 0387715177. URL http://books.google.com/books?hl=en&lr=&id=bkaiJabpguUC&pgis=1. 1.1

[9] B Geiger. A 130K protein from chicken gizzard: its localization at the termini of microfilament bundles in cultured chicken cells. *Cell*, 18(1):193–205, September 1979. ISSN 0092-8674. URL http://www.ncbi.nlm.nih.gov/pubmed/574428. 1.3.5

[10] Holger Gerhardt and Christer Betsholtz. Endothelial-pericyte interactions in angiogenesis. *Cell and tissue research*, 314(1):15–23, October 2003. ISSN 0302-766X. doi: 10.1007/s00441-003-0745-x. URL http://www.ncbi.nlm.nih.gov/pubmed/12883993. 1.3.2

[11] David G Greenhalgh. The role of apoptosis in wound healing. *The International Journal of Biochemistry & Cell Biology*, 30(9):1019–1030, September 1998. ISSN 13572725. doi: 10.1016/S1357-2725(98)00058-2. URL http://dx.doi.org/10.1016/S1357-2725(98)00058-2. 1.4

[12] Maria Margarida Dias Soares Quinas Guerra. *Novel approach to vascular network modeling in 3D*. PhD thesis, Universidade Coimbra, 2011. URL http://hdl.handle.net/10316/15836. 1.5

[13] Lars Jakobsson, Claudio a Franco, Katie Bentley, Russell T Collins, Bas Ponsioen, Irene M Aspalter, Ian Rosewell, Marta Busse, Gavin Thurston, Alexander Medvinsky, Stefan Schulte-Merker, and Holger Gerhardt. Endothelial cells dynamically compete for the tip cell position during angiogenic sprouting. *Nature cell biology*, 12(10):943–53, October 2010. ISSN 1476-4679. doi: 10.1038/ncb2103. URL http://www.ncbi.nlm.nih.gov/pubmed/20871601. 1.4.2, 3.2

[14] Y Kubota, H K Kleinman, G R Martin, and T J Lawley. Role of laminin and basement membrane in the morphological differentiation of human endothelial cells into capillary-like structures. *The Journal of Cell Biology*, 107(4):1589–1598, 1988. doi: 10.1083/jcb.107.4.1589. URL http://jcb.rupress.org/content/107/4/1589.abstract. 1.3.4

[15] Vinay Kumar, Abul K. Abbas, and Nelson Fausto. *Robbins & Cotran: Pathologic Basis of Disease*. Saunders, 7th edition, 2004. ISBN 0721601871. 1.3.4

[16] Laurent Lamalice, Fabrice Le Boeuf, and Jacques Huot. Endothelial cell migration during angiogenesis. *Circulation research*, 100(6):782–94, March 2007. ISSN 1524-4571. doi: 10.1161/01.RES.0000259593.07661.1e. URL http://www.ncbi.nlm.nih.gov/pubmed/17395884. 1.3.6, 1.3.6, 1.4.2

[17] Juan Li, ZhiZhong Sun, and Xuan Zhao. A three level linearized compact difference scheme for the Cahn-Hilliard equation. *Science China Mathematics*, 55(4):805–826, August 2011. ISSN 1674-7283. doi: 10.1007/s11425-011-4290-x. URL http://www.springerlink.com/index/10.1007/s11425-011-4290-x. 2.1

[18] Jie Liu and Sudha Agarwal. Mechanical signals activate vascular endothelial growth factor receptor-2 to upregulate endothelial cell proliferation during inflammation. *Journal of immunology (Baltimore, Md. : 1950)*, 185(2):1215–21, July 2010. ISSN 1550-6606. doi: 10.4049/jimmunol.0903660. URL http://www.ncbi.nlm.nih.gov/pubmed/20548028. 1.4.2, 2.5

[19] Anthony Mescher. *Junqueira's Basic Histology: Text and Atlas, 12th Edition*. McGraw-Hill Medical, 12 edition, 2009. URL http://www.amazon.co.uk/Junqueiras-Basic-Histology-Atlas-Edition/dp/0071630201. 1.3.1

[20] Florian Milde, Michael Bergdorf, and Petros Koumoutsakos. A hybrid model for three-dimensional simulations of sprouting angiogenesis. *Biophysical journal*, 95(7):3146–60, October 2008. ISSN 1542-0086. doi: 10.1529/biophysj.107.124511. URL http://www.cell.com/biophysj/fulltext/S0006-3495(08)78459-5. 1.5

[21] T J Mitchison and L P Cramer. Actin-based cell motility and cell locomotion. *Cell*, 84(3):371–9, February 1996. ISSN 0092-8674. URL http://www.ncbi.nlm.nih.gov/pubmed/8608590. 1.3.6

[22] Joseph E Olberding, Michael D Thouless, Ellen M Arruda, and Krishna Garikipati. The non-equilibrium thermodynamics and kinetics of focal adhesion dynamics. *PloS one*, 5(8):e12043, January 2010. ISSN 1932-6203. doi: 10.1371/journal.pone.0012043. URL http://www.pubmedcentral.nih.gov/articlerender.fcgi?artid=2923603&tool=pmcentrez&rendertype=abstract. 1.3.6

[23] Akira Onuki. *Phase Transition Dynamics*. Cambridge University Press, Cambridge, 2002. ISBN 9780511534874. doi: 10.1017/CBO9780511534874. URL http://ebooks.cambridge.org/ref/id/CBO9780511534874. 1.2

[24] Y Oono. Study of phase-separation dynamics by use of cell dynamical systems. *Physical Review A*, 38(1), 1988. URL http://repository.ias.ac.in/32406/. 2.1

[25] J.S. Penn, editor. *Retinal and Choroidal Angiogenesis*. Springer Netherlands, Dordrecht, 2008. ISBN 978-1-4020-6779-2. doi: 10.1007/978-1-4020-6780-8. URL http://www.springerlink.com/content/k6382p173n17v805/. 1.1

[26] Axel R Pries, Michael Höpfner, Ferdinand le Noble, Mark W Dewhirst, and Timothy W Secomb. The shunt problem: control of functional shunting in normal and tumour vasculature. *Nature reviews. Cancer*, 10(8):587–93, August 2010. ISSN 1474-1768. doi: 10.1038/nrc2895. URL http://www.pubmedcentral.nih.gov/articlerender.fcgi?artid=3109666&tool=pmcentrez&rendertype=abstract. 1.5

[27] Lorenz Ratke and Peter W. Voorhees. *Growth and Coarsening: Ostwald Ripening in Material Processing (Google eBook)*. Springer, 2002. ISBN 3540425632. URL http://books.google.com/books?id=baKRnEuSBXkC&pgis=1. 2.1, A

[28] Yan-Ting Shiu, Jeffrey A Weiss, James B Hoying, Matthew N Iwamoto, In Suk Joung, and Cole T Quam. The role of mechanical stresses in angiogenesis. *Critical reviews in biomedical engineering*, 33(5):431–510, January 2005. ISSN 0278-940X. URL http://www.ncbi.nlm.nih.gov/pubmed/16000089. 1.5

[29] Dan T. Simionescu and Agneta Simionescu, editors. *Vasculogenesis and Angiogenesis – from Embryonic Development to Regenerative Medicine*. InTech, 2011. ISBN 9789533078823. URL http://www.intechopen.com/books/vasculogenesis-and-angiogenesis-from-embryonic-development-to-regenerative-medicine. 1.1, 1.4

[30] RDM Travasso. The Mechanics of Blood Vessel Growth. *cdn.intechopen.com*, pages 1–18, 2007. URL http://cdn.intechopen.com/pdfs/23047/InTech-The_mechanics_of_blood_vessel_growth.pdf. 1.1, 1.4, 1.4.1, 4

[31] Rui D M Travasso, Eugenia Corvera Poiré, Mario Castro, Juan Carlos Rodríguez-Manzaneque, Juan Carlos Rodrguez-Manzaneque, and A Hernández-Machado. Tumor angiogenesis and vascular patterning: a mathematical model. *PloS one*, 6(5):e19989, January 2011. ISSN 1932-6203. doi: 10.1371/journal.pone.0019989. URL http://dx.plos.org/10.1371/journal.pone.0019989. 1.1, 1.5, 2.5

[32] R Zaidel-Bar, M Cohen, L Addadi, and B Geiger. Hierarchical assembly of cell-matrix adhesion complexes. *Biochemical Society transactions*, 32(Pt3):416–20, June 2004. ISSN 0300-5127. doi: 10.1042/BST0320416. URL http://www.ncbi.nlm.nih.gov/pubmed/15157150. 1.3.5

[33] Xiaoming Zheng and GY Koh. Angiogenesis: initiation, extension, and maturation of new blood vessels modulated by vascular endothelial growth factor, angiopoietins, platelet-derived growth. *people.cst.cmich.edu*, X(0), 2012. URL http://people.cst.cmich.edu/zheng1x/Zheng_Koh_Jackson_Final_April_26_2012.pdf. 1.1

[34] Shiwei Zhou and Michael Yu Wang. Multimaterial structural topology optimization with a generalized Cahn–Hilliard model of multiphase transition. *Structural and Multidisciplinary Optimization*, 33(2):89–111, July 2006. ISSN 1615-147X. doi: 10.1007/s00158-006-0035-9. URL http://www.springerlink.com/index/10.1007/s00158-006-0035-9. 2.1, 2.1, 2.1